Remote Sens. **2012**, *4*, 1-x manuscripts; doi:10.3390/rs40x000x

OPEN ACCESS

Remote Sensing

ISSN 2072-4292

www.mdpi.com/journal/remotesensing

Article

Simulations of Infrared Radiances Over a Deep Convective Cloud System Observed During TC4: Potential for Enhancing Nocturnal Ice Cloud Retrievals

Patrick Minnis [1,*], Gang Hong [2], J. Kirk Ayers [2], William L. Smith, Jr. [1], Christopher R. Yost [2], Andrew J. Heymsfield [3], Gerald M. Heymsfield [4], Dennis L. Hlavka [5], Michael D. King [6], Errol Korn [3], Matthew J. McGill [4], Anne M. Thompson [7], Lin Tian [8], and Ping Yang [9]

1 NASA Langley Research Center, Hampton, Virginia, USA; p.minnis@nasa.gov (F.L.); william.l.smith@nasa.gov

2 Science Systems and Applications, Inc., Hampton, Virginia, USA; gang.hong@nasa.gov; (F.L.); j.k.ayers@nasa.gov (F.L.); christopher.r.yost@nasa.gov

3 National Center for Atmospheric Research, Boulder, Colorado, USA; heysm1@ucar.edu; korn@ucar.edu

4 NASA Goddard Space Flight Center, Greenbelt, Maryland, USA; gerald.m.heymsfield@nasa.gov; matthew.j.mcgill@nasa.gov

5 Science Systems and Applications, Inc., Greenbelt, Maryland, USA; dennis.l.hlavka@nasa.gov

6 LASP, University of Colorado, Boulder, Colorado, USA; Michael.king@lasp.colorado.edu

7 Pennsylvania State University, State College, Pennsylvania, USA; amt16@meteo.psu.edu

8 Morgan State University, Baltimore, Maryland, USA; lin.tian-1@nasa.gov

9 Texas A&M University, College Station, Texas; pyang@ariel.met.tamu.edu

* Author to whom correspondence should be addressed; E-Mail: p.minnis@nasa.gov (F.L.); Tel.: +1-757-864-5671; Fax: +1-757-864-7996.

Received:

Abstract: Retrievals of ice cloud properties using infrared measurements at 3.7, 6.7, 7.3, 8.5, 10.8, and 12.0 μm can provide consistent results regardless of solar illumination, but are limited to cloud optical thicknesses $\tau < \sim 6$. This paper investigates the variations in radiances at these wavelengths over a deep convective cloud system for their potential to extend retrievals of τ and ice particle size D_e to optically thick clouds. Measurements from the Moderate Resolution Imaging Spectroradiometer Airborne Simulator—ASTER, the Scanning High-resolution Interferometer Sounder, the Cloud Physics Lidar (CPL), and the Cloud Radar System (CRS) aboard the NASA ER-2 aircraft during the NASA TC4

(Tropical Composition, Cloud and Climate Coupling) experiment flight during 5 August 2007, are used to examine the retrieval capabilities of infrared radiances over optically thick ice clouds. Simulations based on coincident *in-situ* measurements and combined cloud τ from CRS and CPL measurements are comparable to the observations. They reveal that brightness temperatures at these bands and their differences (BTD) are sensitive to τ up to ~20 and that for ice clouds having τ > 20, the 3.7 – 10.8 μm and 3.7 – 6.7 μm BTDs are the most sensitive to D_e. Satellite imagery appears consistent with these results.

Keywords: clouds; optical depth; particle size; satellite; TC4; multispectral thermal infrared

1. Introduction

Ice clouds occur up to 70% of the time in the tropical tropopause region [1]. Upper tropospheric ice clouds reduce the solar radiation reaching the Earth by reflecting a portion of the incoming solar radiation back into space. On the other hand, through the absorption of a portion of the upwelling IR radiation emitted by the lower atmosphere and the Earth's surface, and by the emission of IR radiation at a lower temperature, ice clouds heat the atmosphere and reduce the outgoing longwave radiation [2]. It has been found that the net radiative effect of tropical ice clouds depends on their micro/macro physical and optical properties [3]. Besides their significant impacts on the radiation balance, ice clouds play important roles in the physical and chemical processes occurring in the Tropical Tropopause Layer (TTL) and the stratosphere ([4] and references therein). Additionally, ice clouds, especially those that are optically thick, play important roles in the atmospheric water and latent heat budgets as well as precipitation processes. Knowledge of the formation, maintenance, and properties of these clouds is fundamental for understanding the influences of upper tropospheric ice clouds on these processes (e.g., [5-7]).

Because of their favorable spatial and temporal coverage, passive satellite visible, shortwave−infrared, and infrared (IR) measurements have been extensively used to retrieve optical and micro/macro physical properties of ice clouds (e.g., [8-16]). The shortwave-infrared bands centered at 1.6, 2.1, and 3.7 μm, in general, are sensitive to cloud effective particle size D_e, whereas the nearly non-absorbing bands centered at 0.65, 0.86, and 1.2 μm are primarily sensitive to cloud optical thickness τ. Combinations of these bands (or/and IR bands) have been used to simultaneously retrieve cloud τ and D_e during daytime [e.g., [8-9] [12] [15]). For example, the bands at 0.65, 0.86, 1.24, 1.64, 2.13, and 3.75 μm included in the Moderate Resolution Imaging Spectroradiometer (MODIS) instruments on board the Terra and Aqua satellites have been used for operational retrievals of cloud τ and D_e [9] [15]. The bands at 0.63, 0.87, 1.6/3.75, 10.8, and 12.0 μm, which comprise the Advanced Very High Resolution Radiometer (AVHRR) complement on the National Oceanic and Atmospheric Administration (NOAA) satellites, have been used operationally in the NOAA extended Clouds from AVHRR (CLAVR)-x processing system [17-18]. A unique set of cloud detection and retrieval algorithms was developed by Minnis et al. for the NASA Clouds and Earth's Radiant Energy System (CERES, [19]) Project utilizing as few channels as possible while producing consistent and accurate cloud properties among various satellite sensors including MODIS and imagers on geostationary

satellites [12] [20]. In their daytime retrieval algorithms, the Visible Infrared Shortwave-infrared Split-Window Technique (VISST) based on 0.65, 3.75, and 10.8-μm bands is for snow-free surfaces and the Shortwave-infrared Infrared Near-infrared Technique (SINT) based on 1.6/2.1, 3.75, and 10.8-μm bands for snow or ice-covered surfaces.

The diurnal variations of ice cloud properties are an important element for understanding the earth radiation and latent heat budget. Accurately understanding the diurnal variations of ice cloud properties is crucial for improving numerical weather and climate modeling (e.g., [21-24]). Thus, retrieval of ice cloud properties during nighttime is essential for accurately defining their role in climate.

Passive satellite IR measurements have been extensively used to estimate ice cloud τ, D_e and other cloud properties during both day and night (e.g., [11-12] [16] [25]). A split-window technique using 10.8 and 12.0-μm bands was proposed by Inoue and Wu to estimate cloud temperature and emissivity [26-27]. Since then, the split-window method has been used to detect cloud types and estimate cloud properties extensively ([16] and references therein). A tri-spectral combination of observations at 8.5, 10.8, and 12.0 μm bands has been used to detect ice clouds and estimate ice cloud properties (e.g., [28-30] and references therein). Dubuisson et al. investigated the sensitivity of 8.7, 10.6, and 12.0 μm radiances, measured by the CALIPSO Imaging Infrared Radiometer, to ice cloud τ and D_e and found that the 8.7-μm band improves the retrievals of non-opaque ice cloud τ and D_e [30].

The cloud emittance at 3.7 μm was found to be more sensitive to changes in cloud τ and D_e than at 10.8 and 12.0 μm [11-12] [31-32]. Lin and Coakley retrieved semitransparent cloud D_e using IR measurements at 3.7, 10.8, and 12.0 μm [33]. Ou et al. developed a method to derive cirrus cloud temperature (T_c), τ, and D_e from nighttime AVHRR measurements of brightness temperatures at 3.7 and 10.9 μm [34]. Brightness temperature differences between the 3.7 (including reflected solar radiance) and 10.8 μm bands were used to estimate cloud D_e at the tops of tropical deep convective clouds [35]. An operational method, the Shortwave-infrared Infrared Split-window Technique (SIST), was developed for retrieving T_c, τ, and D_e by Minnis et al. over all surfaces using BTDs between 3.7 and 10.8 μm and between 10.8 and 12.0 μm [11-12]. Moreover, the SIST provides consistency between day and night for retrievals of semitransparent cloud properties and consistency among various satellite sensors because the three bands were included in most geostationary and polar-orbiting satellite imagers, such as NOAA AVHRR and the Geostationary Operational Environmental Satellites (GOES) imager.

The water vapor band at 6.5 μm and window band at 11.5 μm were used to derive T_c and the emissivity of semitransparent cirrus clouds by Szejwach [36]. Liou et al. used 6.5 and 10.5 μm for retrieving tropical cirrus cloud T_c and τ for $\tau < 6$ [37]. The 6.7/7.3-μm bands have been also used for assisting MODIS cloud detection during nighttime [38-40]. Lutz et al. found that involving 3.9 and 6.2-μm bands improved a cloud classification method that is only based on the split-window technique [41].

Satellite high-spectral resolution IR observations, which provide rich information content for retrieving a variety of atmospheric parameters, have also been used to infer ice cloud properties [42] [43-46]. The high-resolution spectra of the Atmospheric Infrared Sounder (AIRS) aboard the Aqua satellite were used to retrieve cirrus τ and D_e [43-44]. Huang et al. found that the slope of brightness temperature in the AIRS 750–1000-cm^{-1} region is sensitive to small D_e and the spectrum in the 1100–

1250-cm^{-1} region is more sensitive to τ than to D_e [42]. In addition to these channels, Wei et al. found that BTDs between 900.562-cm^{-1} band (11.1 μm, atmospheric window) and 1558.692-cm^{-1} band (6.42 μm, strong water vapor absorption) and between 1587.495-cm^{-1} (6.3 μm, moderate water vapor absorption) and 1558.692-cm^{-1} band (6.42 μm) are sensitive to semitransparent ice cloud values of τ [45]. A selection of 14 channels in the 800–1130-cm^{-1} thermal IR window of AIRS has also been used to infer cirrus τ and D_e [46].

As noted above, IR retrieval algorithms have been extensively developed for estimating ice cloud properties, but reliable IR retrievals of τ and D_e are limited to non-opaque clouds having τ less than ~6 [12] [37] [47]. Thick ice clouds often occur with distinct differences in their daytime and nocturnal frequencies. Thus, monitoring of the diurnal cycle of ice cloud properties such as τ, D_e, and ice water path (IWP) is currently limited to daylight observations only. To begin the process of addressing this shortcoming, this study investigates the IR signals from optically thick ice clouds using campaign measurements and rigorous radiative transfer modeling to determine the potential for estimating optically thick ice cloud τ and D_e using selected IR bands at 3.7, 6.7, 7.3, 8.5, 10.8, and 12.0 μm. These bands are among the channels on many geostationary and/or polar meteorological satellite imagers.

Section 2 describes the detailed measurements from the NASA ER-2 and DC-8 aircraft and radiosonde ascents for a case study of a tropical deep convective cloud system observed during the Tropical Composition, Cloud and Climate Coupling Experiment (TC4) on 5 August 2007 [48]. The measurements include cloud vertical profiles made by a cloud radar and lidar, ice cloud particle sizes and habits from *in situ* probes, and radiances made by an airborne scanning spectrometer covering visible to IR bands and an airborne scanning high-resolution IR interferometer. Using observations and simulations, section 3 examines the effects of τ and D_e on upwelling IR radiances over the tropical deep convective cloud system. The measurements from the airborne scanning high-resolution IR interferometer are used to construct IR brightness temperatures at the MODIS bands of 3.7, 6.7, 7.3, 8.5, 10.8, and 12.0 μm. Simulations are based on a rigorous radiative transfer model with inputs of *in situ* atmospheric profiles and cloud microphysical and optical properties derived from airborne measurements. Gamma particle size distributions are also used in simulations for the aim of investigating the influence of D_e on IR radiances. Section 4 summarizes this study.

2. Combined Measurements over a Deep Convective Cloud System

The TC4 experiment was conducted from Costa Rica during July and August 2007 to study the relationships among upper level clouds, aerosols, chemistry, and radiation to better understand the TTL [48]. GOES-10 and GOES-12 data were used to direct the flights and determine the large-scale environment and progress of deep convection (http://www-angler.larc.nasa.gov/TC4). This study focuses on a particular convective cloud system observed during 5 August 2007, when the ER-2 and DC-8 executed more than 4 hours of flights at their respective cruising altitudes of about 20 and 10 km. The coordinated flight segment between 1350 and 1438 UTC is the focus of this study.

Because of its high altitude, the ER-2 effectively serves as a satellite having an array of remote sensing instruments. The MODIS/Advanced Spaceborne Thermal Emission and Reflection Radiometer, ASTER (MASTER) on the ER-2 measured radiances at most of the satellite imager

wavelengths of interest. The MASTER is a cross-track scanning spectrometer that measures reflected solar and emitted thermal radiation in 50 narrowband channels in the range 0.4 - 13 μm. Its 2.5-mrad instantaneous field of view (FOV) results in a spatial resolution at nadir of 50 m at the nominal ER-2 altitude of 20 km. At that altitude, the total FOV of the MASTER is 85.92º (±42.96º from nadir), which yields a ground swath of about 37.25 km. The MASTER is described in detail by [49] and [50]. The IR radiances observed by MASTER bands 30 (3.7 μm), 43 (8.6 μm), 48 (11.3 μm), and 49 (12.2 μm) are used in this study.

During TC4 the MASTER lacked the water vapor bands at 6.7 and 7.3 μm that are currently carried on the MODIS. In this study, the measurements from the Scanning High-resolution Interferometer Sounder (S-HIS) on the ER-2 are used to construct radiances in the 6.7 and 7.3 μm bands that are available on the MODIS. The S-HIS is a scanning interferometer which measures emitted thermal radiation at high spectral resolution between 3.3 and 18 μm [51]. Its instrument FOV is 100 mrad and its total view angle is ±30º, so from the ER-2 it produces sounding data with 2 km resolution at the nadir and covers a 40-km ground swath.

The ER-2 carried the CRS and CPL which are well suited for ice cloud studies because of their high sensitivities and spatial resolutions. The CRS [52] is a 94-GHz (W-band, 3.2 mm wavelength) pulsed polarimetric Doppler radar. It was designed to provide nadir cloud profiling from the ER-2. The ER-2 CRS measurements have a vertical resolution of 37.5 m and temporal resolution of 0.5 s. The minimum detectable reflectivity is -28 dBZ for the CRS at a range of 15 km from the ER-2. Because the CRS minimum detectable reflectivity is limited, the CRS measurements could miss the tops of ice clouds with small ice particles. Lidar measurements are used to observe the clouds missed by the CRS since lidar is more sensitive to small ice particles and optically thin cirrus cloud than radar. McGill et al. used the CPL to profile optically thin cirrus clouds frequently missed by the CRS during the Cirrus Regional Study of Tropical Anvils and Cirrus Layers – Florida Area Cirrus Experiments in July 2002 [53]. It was found that the τ missed by the CRS, but detected by the CPL, is in the range of 0.15-0.45. The CPL is a backscatter lidar with three wavelengths of 0.355, 0.532, and 1.064 μm [53-54]. It scans downward from the ER-2 with a vertical resolution of 30 m and a 1 s temporal resolution, which is about 200 m at an average ER-2 ground speed of about 200 ms^{-1}. Only the CPL measurements at 0.532 μm over the deep convective cloud system are used in this study.

The DC-8 carried several cloud particle size probes to take *in situ* measurements and dropsondes to obtain temperature and humidity profiles below the aircraft. Ice cloud bulk scattering properties are mainly dependent on ice particle habits and ice cloud particle size distributions. Combined measurements from the 2-Dimensional Stereo (2D-S) probe, 2D Cloud Imaging Probe (CIP), and Precipitation Imaging Probe (PIP) on the DC-8 are used to construct ice cloud particle size distributions covering size bins from 5 μm to 6 mm in the present study.

Numerous small ice particles (maximum dimension D less than 50 μm) have been observed in ice clouds by *in situ* measurements. However, large portions of these small ice particles could be generated by large crystals shattering on the inlets of instruments such as the Forward Scattering Spectrometer Probe (FSSP) and others which ingest ice particles into sample volumes through inlets ([55] and references therein). The 2D-S uses detector arms instead of an inlet tube to minimize shattering fragments from entering the sample volume, however, collisions of the ice crystals and the forward elements of the probe still introduce some significant uncertainties into the derived size

distributions [56] [57]. It detects particles as small as 10 μm (the minimum size bin is 5-15 μm) [56]. For the TC4 dataset, the maximum particle size bin that produced adequate sampling statistics was about 3000 μm.

The CIP measured particle sizes ranging from about 50-100 μm to more than 1 mm, and the PIP measured particles sizes from about 100 μm to 6 mm [58]. Although both instruments nominally provide a minimum detectable size of 50 μm, the lowest detection threshold from the CIP was suggested to be 100 μm during TC4 because of uncertainties in the probe's sample volume [58-60]. Jensen et al. found that the size distributions derived from the CIP agree well with those from the 2D-S imaging instruments for the size bins above 100-200 μm despite the uncertainties in both instruments' sample volume sizes [55]. For detailed information on the CIP and PIP, see Tian et al. who investigated cirrus ice particle size distributions using TC4 CIP and PIP observations [60].

The CPI can image particles in the size range of 15-2500 μm with a nominal 2.3 μm resolution [56]. During TC4, the CPI aboard the DC-8 had 33 size bins between 0 and 1000 μm. The particle densities of seven habit categories including sphere, column, plate, rosette, budding rosette, small and large irregular particles were measured separately for ice particles with $D < 50$ μm and $D > 50$ μm. The habit mixtures derived with an automated technique from the measured number densities are used for computing ice cloud bulk scattering properties. Although all of the probe measurements have some significant uncertainties, they still provide the most realistic estimate of the microphysical properties of the clouds in this system and, should yield reasonable estimates of the radiances.

Figure 1 shows a combined GOES-10 and GOES-12 IR 10.8-μm brightness temperature image over the TC4 domain at 1558 UTC on August 5, 2007. Coordinated flights of the ER-2 over and the DC-8

Figure 1. Infrared (10.8 μm) brightness temperatures from combined GOES-10 and GOES-12 data over the TC4 domain, 1558 UTC, 5 August 2007, with ER-2 (blue) and DC-8 (red) flight tracks. Flight altitudes are shown as a function of UTC time in the lower left inset.

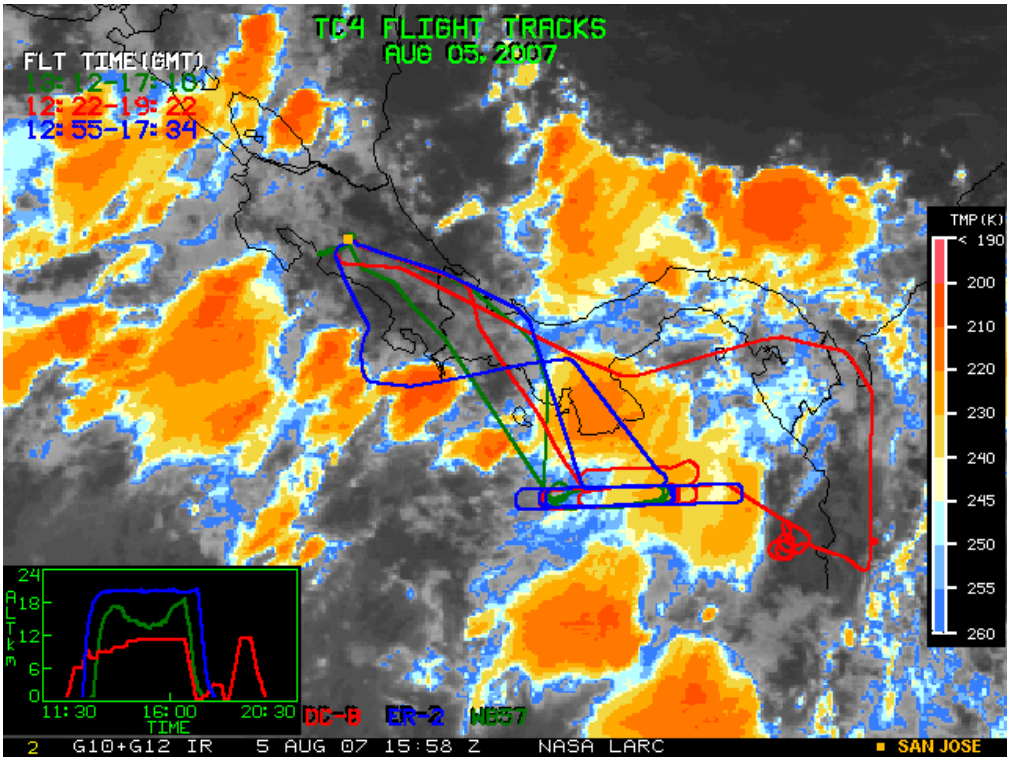

Figure 2. (a). MODIS/ASTER airborne simulator (MASTER) RGB images for flight tracks, 1350-1440 UTC, 5 August 2007 (blue: ER-2, red: DC-8, green: ER-2 during turn). (b). CRS reflectivity for the deep convective cloud system along the ER-2 flight track. CPL-detected cloud tops for the upper two layers are shown by the red and brown lines, respectively. CPL-detected cloud bases for the upper two layers are shown in black and gray lines, respectively. Gap corresponds to the ER-2 turn.

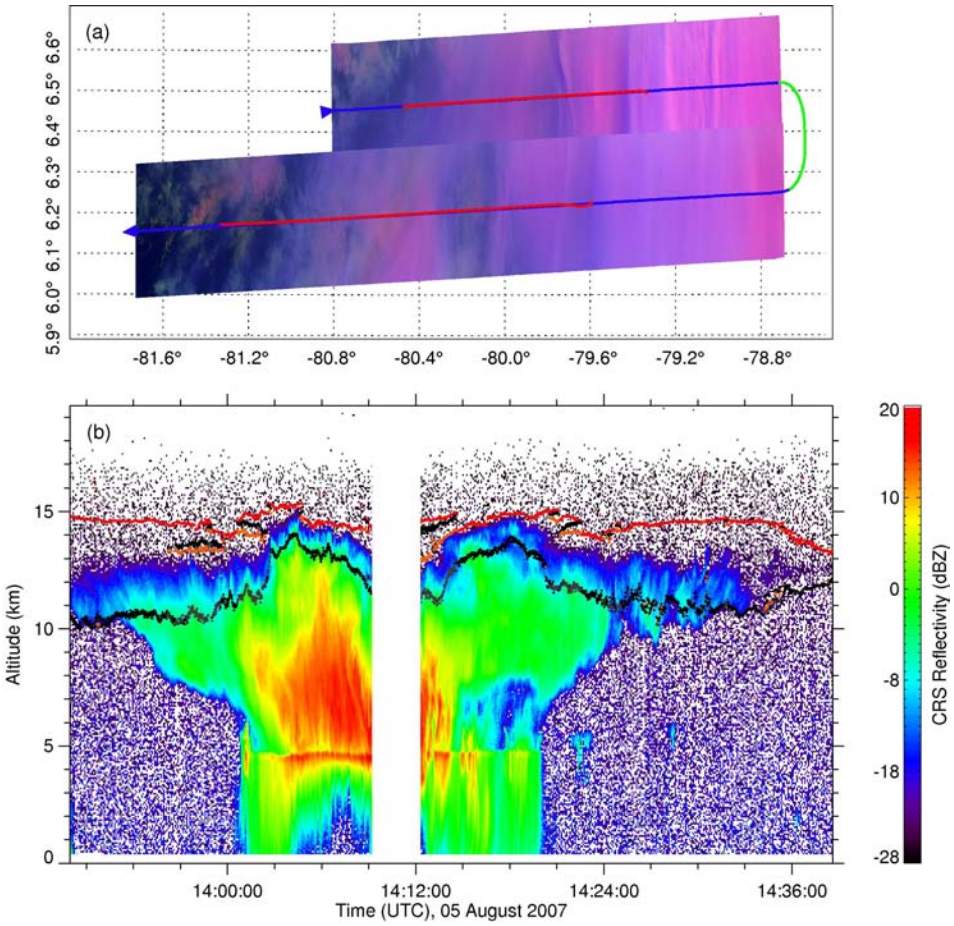

in the clouds followed an east-west orientation in the Panama Bight at about 6.5°N, where an anvil cirrus was observed flowing from a deep convective core at about 79°W. One coordinated segment for the ER-2 and DC-8 over the anvil cirrus and deep convective core occurred from about 13:50 to 14:40 UTC (ER-2 flight) which is shown in Figure 2a together with the MASTER false color RGB image. The MASTER false RGB image is based on the band 5 (0.66 μm) reflectance, band 21 (2.16 μm) reflectance, and band 48 (11 μm) brightness temperatures with the scale reversed. The ocean background is dark in the false color image. Optically thick ice clouds including the anvil and the upper part of the deep convective core are purple. Thin cirrus clouds are light blue. Note that only the DC-8 tracks (in red) coordinated with the ER-2 track (in blue) are shown here. During the west-to-east leg, the DC-8 flight had a lag of about 7-8 minutes with respect to the ER-2, while along the east-to-west leg, the ER-2 lagged the DC-8 by about 6-7 minutes. Figure 2b shows the cloud vertical cross section given by the CRS reflectivity along the ER-2 track. Cloud top and base detected by the CPL for the upper two layers of ice clouds are also shown in Figure 2b. The vertical structure of the CRS reflectivity distinctly shows the outflow anvil cirrus from the deep convection.

The DC-8 launched four dropsondes along the track shown in Figure 2: (79.49°W, 6.50°N) at 13:54:06 UTC, (80.86°W, 6.19°N) at 14:10:19 UTC, (79.68°W, 6.49°N) at 14:23:24 UTC, and

Figure 3. Mean atmospheric water vapor and temperature profiles (with -1 K shifting) from four DC-8 dropsondes (see text for details) along the track shown in Figure 2. The atmospheric profiles from the surface radiosonde launched at 1505 UTC from the NATIVE site at Las Tablas, Panama (80.25°W, 7.75°N) are also shown together with their smoothed ones.

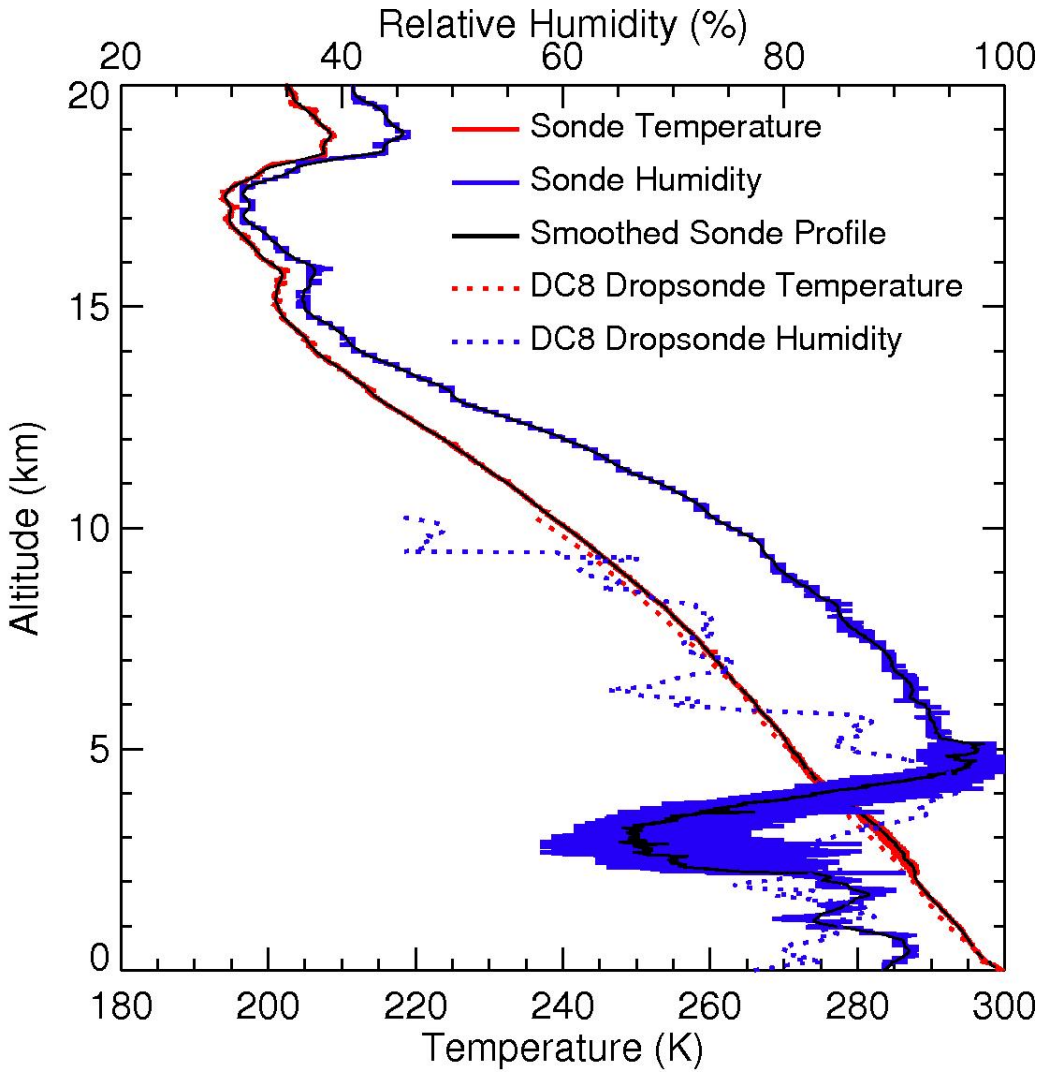

The DC-8 launched four dropsondes along the track shown in Figure 2: (79.49°W, 6.50°N) at 13:54:06 UTC, (80.86°W, 6.19°N) at 14:10:19 UTC, (79.68°W, 6.49°N) at 14:23:24 UTC, and (81.37°W, 6.18°N) at 14:41:32 UTC. Surface radiosonde measurements launched at 15:05 UTC at Las Tablas, Panama (80.25°W, 7.75°N) from the Nittany Atmospheric Trailer and Integrated Validation Experiment (NATIVE) included high vertical resolution profiles of atmospheric temperature, humidity, and ozone mixing ratio [61]. Figure 3 shows the mean profiles of atmospheric water vapor and temperature from the four DC-8 dropsondes and the profiles of temperature and water vapor from the NATIVE ground-based sonde. The mean temperature profile is essentially the same as NATIVE sonde. The mean water vapor profile from the dropsondes is only available below about 10.3 km. Thus, above 10.3 km, the scaled NATIVE water vapor profile is used to complete the mean water vapor profile that is used for the present simulations together with the NATIVE temperature and ozone profiles.

Figure 4. Example of S-HIS spectrum and Aqua MODIS and TC4 MASTER band SRFs around 3.7, 6.7, 7.3, 8.5, 10.8, and 12.0 μm.

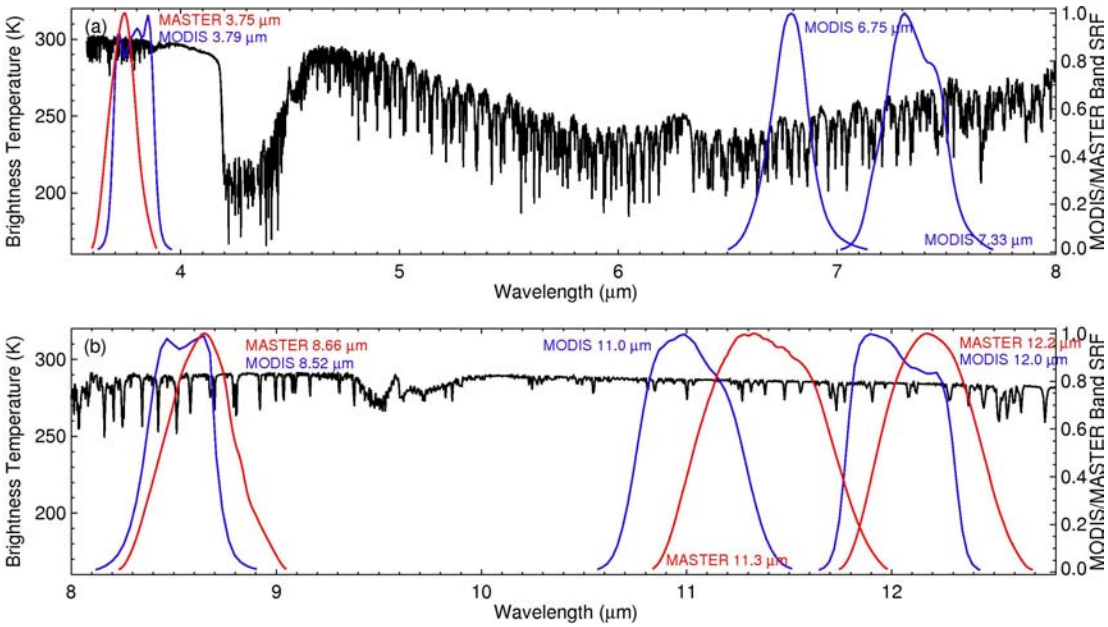

3. Infrared Radiances over the Deep Convective Cloud System: Observations and Simulations

3.1. The S-HIS Derived IR Brightness Temperatures at the MODIS Bands

Although the MASTER has bands similar to the MODIS complement, it has different spectral response functions (SRFs) and lacks a few bands. In particular, it does not have the MODIS water vapor bands at 6.7 and 7.3 μm. Here, the measurements from the S-HIS aboard the ER-2 are used to construct the MODIS bands at 3.7, 6.7, 7.3, 8.5, 10.8, and 12.0 μm. Figure 4 shows an example of an S-HIS spectrum and the Aqua MODIS and TC4 MASTER band SRFs around 3.7, 6.7, 7.3, 8.5, 10.8, and 12.0 μm. The S-HIS measurements and MASTER SRFs at 3.7, 8.5, 10.8, and 12.0 μm were used to construct the pseudo-MASTER brightness temperatures that were then compared to the corresponding observed MASTER brightness temperatures. The matched brightness temperatures, shown in Figure 5, agree well with each other with a standard deviation of ~1 K in their differences. Theoretically, if S-HIS and MASTER have the exact same observation geometry and FOVs, the comparisons should be essentially the same. Similarly, the S-HIS measurements and MODIS SRFs at 3.7, 6.7, 7.3, 8.5, 10.8, and 12.0 μm were used to simulate the MODIS-observed brightness temperatures at these bands (Figure 6). These pseudo-MODIS brightness temperatures are considered as MODIS observations in the present study.

3.2. Optical Thickness Profiles from Combined CRS and CPL Measurements

The CRS measurements are primarily used to obtain vertical cloud τ profiles. Three cloud phases, ice, liquid, and mixed phase, are considered here. The vertical profiles are separated into three layers, ice (top layer), mixed-phase (middle layer), and liquid (bottom layer) clouds. The layer with temperatures less than -20°C is defined as ice cloud, the layer with temperature exceeding 0°C is a liquid cloud. The layer between -20°C to 0°C is the mixed-phase cloud [62]. In the bottom layer, the

Figure 5. Brightness temperatures at 3.75, 8.66, 11.3, and 12.2 μm using the MASTER SRFs applied to S-HIS measurements and MASTER measurements.

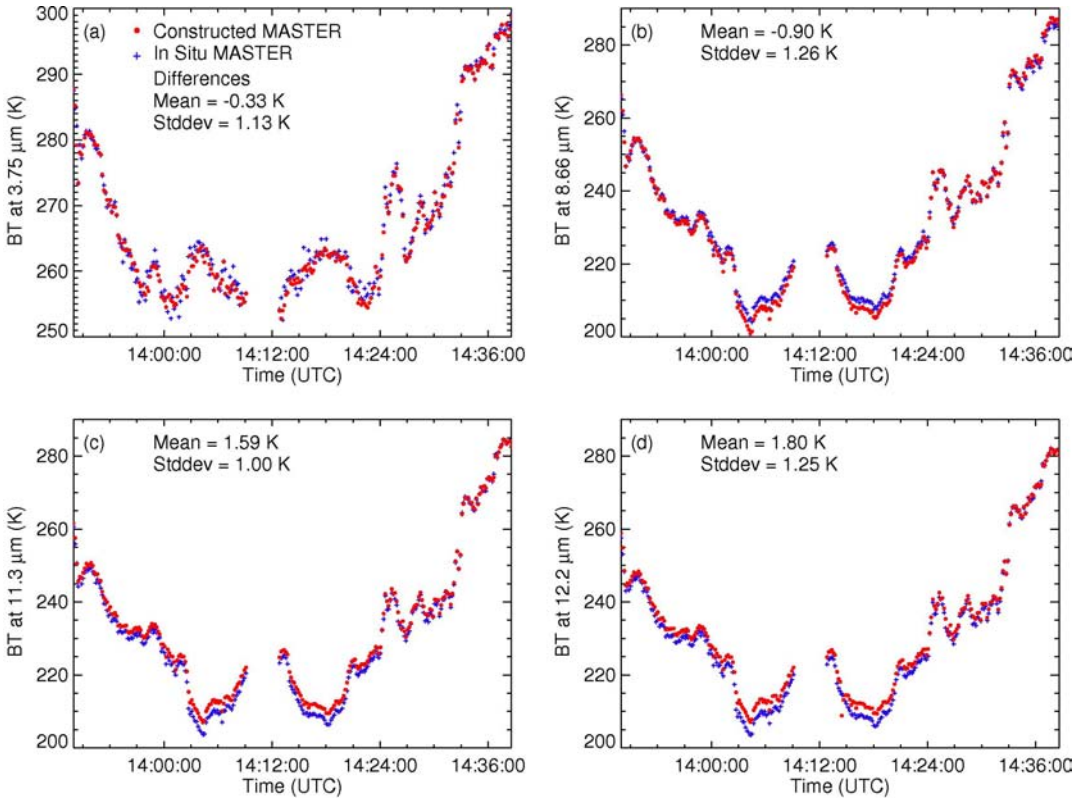

Figure 6. Equivalent MODIS brightness temperatures at 3.79, 6.75, 7.33, 8.52, 10.8, and 12.0 μm along the flight track constructed using MODIS SRFs applied to the S-HIS measurements.

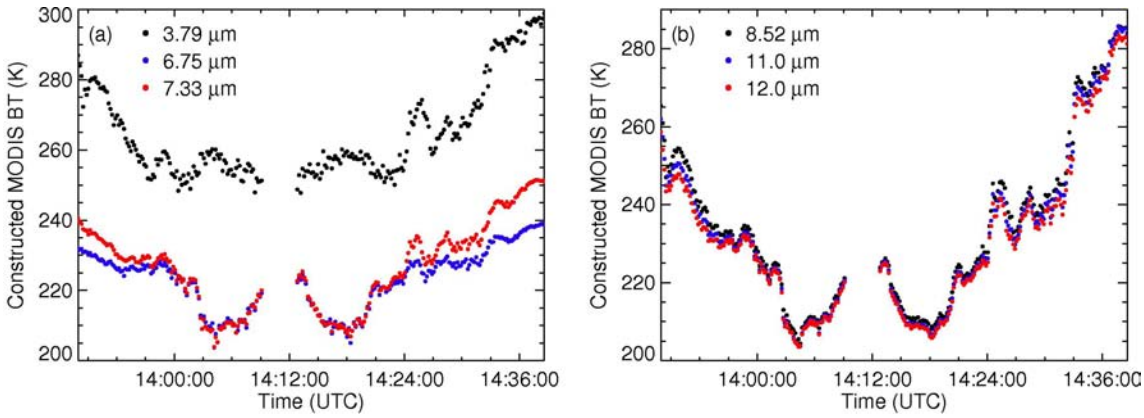

liquid cloud water content (*LWC*) is derived by the Z_e–*LWC* relationship by Baedi et al.,

$$Z_e = 57.54 \cdot LWC^{5.17}, \quad (1)$$

where *LWC* is in g m^{-3} and Z_e is in mm^6 m^{-3}. In the ice cloud, the ice water content (*IWC*) is derived by the Z_e–*IWC* relationship of Liu and Illingworth,

$$IWC = 0.137\, Z_e^{0.643}, \quad (2)$$

where *IWC* and Z_e are in the same units as those for Z_e–*LWC* [63-64].

For the mixed-phase layer, *LWC* is assumed to decrease to 0 linearly with increasing altitude from the freezing level to the bottom of the ice cloud layer. Conversely, *IWC* is assumed to increase linearly from 0 g m^{-3} following Equation (2). On the basis of these assumptions, an ice fraction *IceFra* is defined to separate the two parts of CRS reflectivity, $IceFra = -(t - t_0)/(t_0 - t_{Tra})$, where t is atmospheric temperature in degree, t_0 is the temperature at the freezing level, and t_{Tra} is the transition temperature from mixed-phase to ice cloud. In the present study, 0°C is used for t_0, so $IceFra = t / t_{Tra}$. A phase transition temperature of -20°C (altitude is ~8.3 km) is used. Therefore, the two parts of the CRS reflectivity due to cloud ice Z_e^{ice} and liquid water Z_e^{liq}, are obtained from $Z_e^{ice} = IceFra * Z_e$ and $Z_e^{liq} = (1 - IceFra) * Z_e$, respectively. *IWC* and *LWC* are then obtained by applying Z_e^{liq} and Z_e^{liq} to Equations (1) and (2), respectively. Because of difficulties in separating the surface radar return from the hydrometeors at the first 500 m above the surface, CRS reflectivity below 500 m is assumed to be that at the level of 500 m [65-66].

While the CRS retrieval algorithm assumes the ice fraction varies as indicated above, the Rosemount icing probes detected no liquid water at temperatures up to -3°C for this flight segment. Thus, to provide a more realistic variation of cloud water structure, a second profile was constructed assuming no liquid water for temperatures less than 0°C. Thus, in the 0·to -20°C transition zone used above, *IceFra* is set equal to zero for a second set of calculations. Both results are used to determine the sensitivity of the calculations to the assumptions about supercooled liquid water in the clouds.

The CPL measurements have been used to compensate for the optically thin cirrus part that is missed by the CRS measurements [53]. Figure 7 shows the vertical structure of the deep convective cloud system as seen from the CRS and CPL measurements and the τ profiles constructed from the CRS and CPL data for the pure ice layer. The total optical thicknesses, those from the CPL and those missed by the CRS along the flight track over the cloud system, are also shown in Figure 7. Visible τ from the CRS shown in the Figure 7c is derived from the empirical relationship $\tau = 0.065 \cdot LWP^{0.84}$ for cloud ice and $\tau = 3.0/20.0 \cdot LWP$ for cloud liquid (assuming ice water clouds with D_e = 20 μm and an extinction efficiency, Q_e = 2.0), respectively [12] [67]. The minimum detectable reflectance from the CRS is used to isolate the CPL-measured cloud areas missed by the CRS measurements: overlapping is denoted where the CRS gray region is visible under the CPL color region Figure 7a. The cloudy area missed by the CRS is shown as the gray region in Figure 7b. Figure 8a shows examples of the constructed vertical profiles for ice and liquid cloud τ. One profile is taken from an anvil cloud measured at 13:56:34 UTC, and the other one is taken from a convective core measured at 14:06:10 UTC. The CPL cumulative ice cloud τ that are missed by the CRS measurements along the flight path are detailed in Figure 8b. The τ most frequently missed by the CRS but detected by the CPL is ~0.20. Overall, the average missed τ by the CRS is 0.28 ± 0.17, which is consistent with the values deduced from CRYSTAL-FACE data (0.15-0.45 [53]).

3.3. Cloud Bulk Scattering Properties During the Flight Track

Cloud bulk scattering properties are commonly used to simulate IR radiances emanating from clouds [68-74]. Ice cloud bulk scattering properties are computed by averaging ice particle single scattering properties (i.e., single scattering albedo, absorption and scattering efficiency, asymmetric factor, and scattering phase function) over ice cloud particle size distributions.

Figure 7. (a) CRS-detected vertical structure of the cloud system and CPL-detected cirrus cloud layers, **(b)** vertical distributions of derived CPL τ and CRS τ in the pure ice cloud layer, **(c)** CPL-detected optical thickness of cirrus clouds and the part missed by CRS measurements plotted with total optical thickness from CRS and CPL. The coincident DC8 tracks are shown in **(a)**. Note that there is a time difference of about 6-8 minutes between the DC-8 and ER2 tracks.

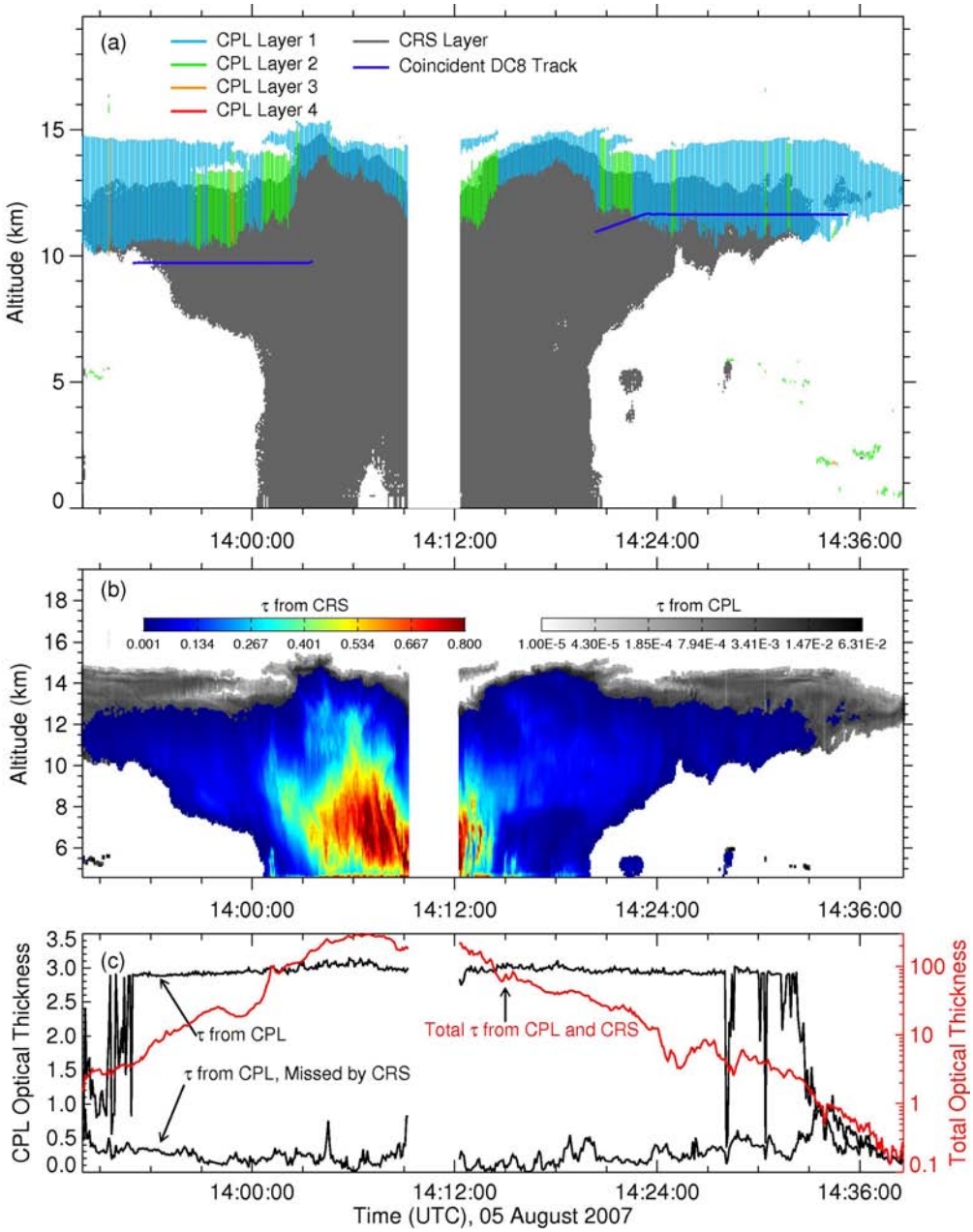

Accurate measurements of ice cloud particle size and habit distributions are crucial for ice cloud bulk scattering properties. In this study, ice cloud particle size distributions from the 2D-S, CIP and PIP measurements are combined to construct the particle size distributions with a minimum size bin of 5-15 μm. To minimize the effects of large-crystal shattering on number densities of small ice particles, the particle size distributions from the 2D-S for small ice particles are combined with those from the CIP and PIP for large ice particles. To be consistent with the CIP and PIP data that have been averaged over 5 seconds or about 1.0 km horizontal path, the 2D-S data are averaged in the same way.

Figure 8. (a) Vertical optical thickness profiles of clouds at 13:56:34 UTC (anvil cloud) and 14:06:10 UTC (convective core), **(b)** occurrences of CPL-derived cumulative ice cloud optical thickness in regions with no CRS detection (minimum detectable sensitivity), August 05, 2007.

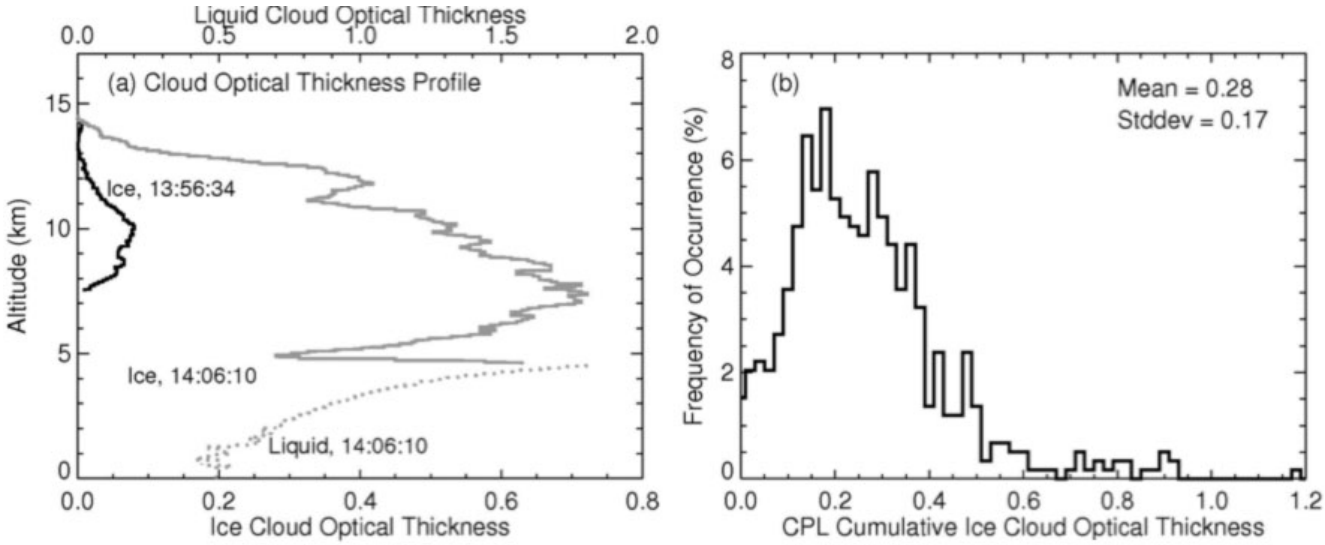

Figure 9 shows the combined ice particle size distributions over an anvil ice cloud and convective core from the 2D-S, CIP, and PIP measurements along the flight track over the deep convective cloud system (Figure 2). High concentrations of small particles are seen in both the anvil at 13:57:09 UTC (Figure 9a) and core at 14:02:07 UTC (Figure 9b). And both cloud types have a second peak concentrated at a maximum dimension D of 200-300 μm. All of the ice particle size distributions along the DC-8 flight track (Figure 7a) are derived and shown in Figure 10. The averaged particle size distribution is used for computing ice cloud bulk scattering properties. Besides the measured particle size distributions, the Gamma particle size distribution [e.g., Kosarev and Mazin [75]) is also used for,

Figure 9. Ice particle size distributions from combined 2D-S, CIP, and PIP measurements for **(a)** a case of cloud anvil (13:57:09 UTC), and **(b)** a case of convective core (14:02:07 UTC) along the flight track.

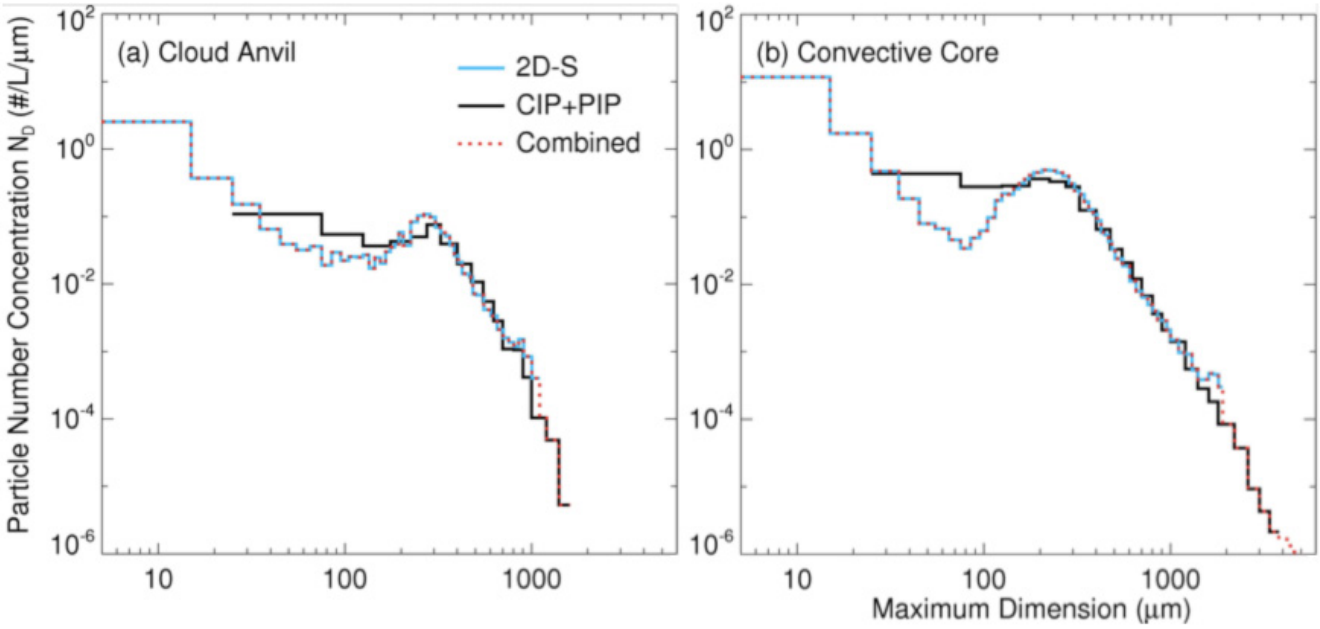

Figure 10. All ice particle size distributions from the 2D-S, CIP, and PIP measurements along the flight track. Mean particle size distribution shown in red.

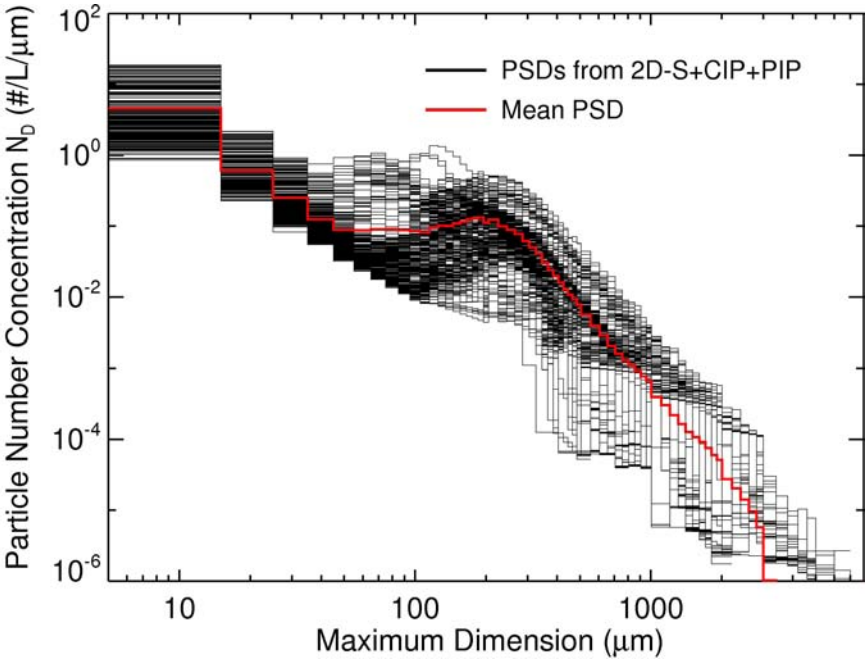

investigating the effects of D_e on the IR radiances from this cloud. The Gamma particle size distribution varies with its parameters, dispersion μ and slope κ. Those used by Hong are adopted here as

$$n(D) = N_0 D^2 \exp(-4.87D/D_0), \quad (3)$$

where N_0 is the intercept and D_0 is the median of the distribution [76].

Also taken from the DC-8, the CPI data were used to resolve the ice cloud particle habits simultaneously with ice particle size distributions during TC4. Using an automatic crystal habit classification program, ice particle shapes measured by the CPI were placed into categories including sphere, column, plate, rosette, budding rosette, and irregular for ice particles with $D < 50$ μm and > 50 μm. Figure 11 shows the ice particle habits detected by the CPI along the flight track. It was found that spherical and irregular particles comprise almost all of the habits when $D < 50$ μm, while the particles with irregular and column habits are most common when $D > 50$ μm. The averaged habit mixing ratios along the flight track are used for computing ice cloud bulk scattering properties. When $D < 50$ μm, the habit distribution consists of 55% spheres, 37% irregular particles, and 8% columns. When $D > 50$ μm, the habit distribution consists of 73% irregular particles, 19% columns, 6% rosettes including rosettes and budding rosettes, 1% spheres, and 1% plates. Single-scattering properties of ice particles with various habits including column, hollow, bullet rosette, plate, aggregate, and droxtal have been investigated extensively (e.g., [71] [74] [77] and references therein). The single-scattering properties of droxtal, column, plate, rosette, and aggregate particles are used respectively for the sphere, column, plate, rosette, and irregular habits determined from the CPI data.

Following Yang et al., the single-scattering properties of ice particles are then averaged over the habit distributions and particle size distributions to obtain ice cloud bulk scattering properties, which are functions of wavelength, and D_e, which is defined by

Figure 11. Ice particle habits detected from the CPI aboard the DC-8 along the ER-2 flight track during August 05, 2007 for ice particles with (a) $D < 50$ μm and (b) $D > 50$ μm. The averaged habit mixing ratios are also shown at the right.

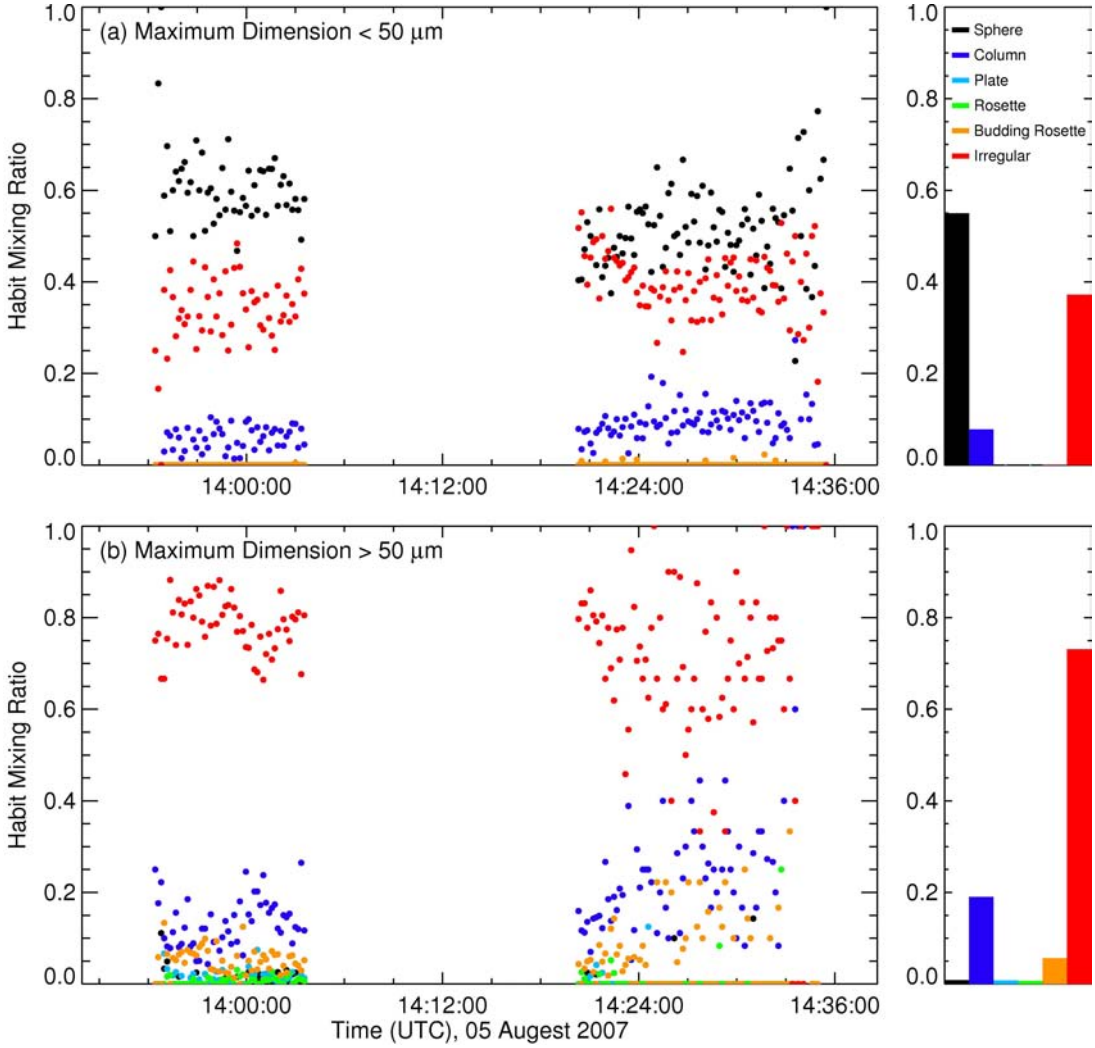

$$D_e = \frac{3}{2} \frac{\int_{D_{\min}}^{D_{\max}} \left[\sum_{i=1}^{N} f_i(D) V_i(D) \right] n(D) \mathrm{d}D}{\left[\sum_{i=1}^{N} f_i(D) A_i(D) \right] n(D) \mathrm{d}D}, \quad (4)$$

where f(D) is the particle habit distribution and $\sum_{i=1}^{N} f_i(D) = 1$, i is index of ice particle habits (total is N) at D, and V and A are particle volume and projected area, respectively [72]. The liquid cloud is assumed to be composed of spherical water droplets. An effective radius r_e of 10 μm with a gamma particle size distribution following Mishchenko and Travis [69] is used for the water cloud bulk scattering properties. For mixed-phase cloud portions (Figure 8a), a water-phase mixing ratio γ is defined by *LWC*/(*IWC*+*LWC*) first, then the bulk scattering properties of mixed-phase clouds are derived by combining those of ice and water clouds [78-81].

3.4. Effects of Optical Thickness and Effective Particle Size on IR Radiances over Tropical Deep Convection

Simulations and observations of the brightness temperatures at 3.7, 6.7, 7.3, 8.5, 10.8, and 12.0 μm (BT_{03}, BT_{06}, BT_{07}, BT_{08}, BT_{11}, and BT_{12}) over the tropical deep convective cloud system are compared to examine the effects of τ and D_e on the IR brightness temperatures.

The set of correlated *k*-distribution routines developed by Kratz [82] and Kratz and Rose [83] for the MODIS bands is used to compute τ for each layer in a clear-sky atmosphere. The atmospheric profiles of temperature and humidity (Figure 3), as well as ozone, are used in the correlated *k*-distribution calculations for each band. The surface emissivity is assumed to be 1.00 for the IR bands. The spectral brightness temperatures over the tropical deep convective cloud systems are then computed with the discrete ordinates radiative transfer model (DISORT; [84]) using the constructed cloud optical thickness profiles (Section 3.2), the computed bulk scattering properties, and various D_e in the range of 10-150 μm.

Figure 12 shows the simulated and observed values of BT_{03}, BT_{06}, BT_{07}, BT_{08}, BT_{11}, and BT_{12} over the subject cloud system as a function of ice cloud τ. The mean particle size distribution (D_e = 95 μm) along the flight track is used for the simulations. Since the measured BT_{03} values include reflected solar radiation while the simulations only include the emitted radiance, the measurements of BT_{03} are not shown in the figure. The other simulated values, BT_{06}, BT_{07}, BT_{08}, BT_{11}, and BT_{12}, generally agree with the corresponding observations. In particular, for optically thick ice clouds with $\tau > 20$, the simulated BT_{06}, BT_{07}, BT_{08}, BT_{11}, and BT_{12} (window bands) values are essentially the same as the observations. For optically thin ice clouds ($\tau < 1$), the simulated BT_{08}, BT_{11}, and BT_{12} are greater than the observations, while the simulated BT_{06}, BT_{07}, BT_{08}, BT_{11}, and BT_{12} are less than the observations for ice clouds having $5 < \tau < 10$ (anvil clouds). These differences are most likely due to the uncertainties in derived ice cloud τ from the CRS (or/and CPL), which can be distinctly different because of the uncertainties in Z_e–LWC relationship [62] [85]. The underlying water clouds tend to decrease the BT_{03}, BT_{08}, BT_{11}, and BT_{12} values for non-opaque ice clouds, but have negligible effect on the water vapor channels' brightness temperatures. The simulations and observations both reveal that BT_{03}, BT_{06}, BT_{07}, BT_{08}, BT_{11}, and BT_{12} are sensitive to ice cloud optical depth for τ up to 20. Furthermore, these sensitivities are essentially monotonic, i.e., these brightness temperatures monotonically decrease with increasing ice cloud optical thickness up to $\tau = 20$. When τ is above 20, the brightness temperatures vary widely although a weak decreasing trend with increasing ice cloud τ is apparent.

The sensitivity of the radiances to phase transition temperature is illustrated in Figure 13, where the 3.7 and 6.7-μm simulations used the -20°C transition temperature (red) and 0° transition (red, same as blue in Figure 12). The results are similar for the other channels (not show). Negligible change is seen in the radiances, but the entire set of radiances is shifted to the right. Thus, the simulated radiances correspond to greater optical depths if it is assumed that the hydrometeors are entirely in the ice phase for T < 0°, as indicated by the in situ data rather than assuming that the layer between 0° and -20°C is a mixture of ice and water as formulated in Sec. 3.2 above. This result is encouraging because the phase of clouds in that temperature range is often uncertain.

Figure 12. Simulated and observed brightness temperatures at 3.7, 6.7, 7.3, 8.5, 10.8, and 12.0 μm over the tropical deep convective cloud system as a function of ice cloud τ.

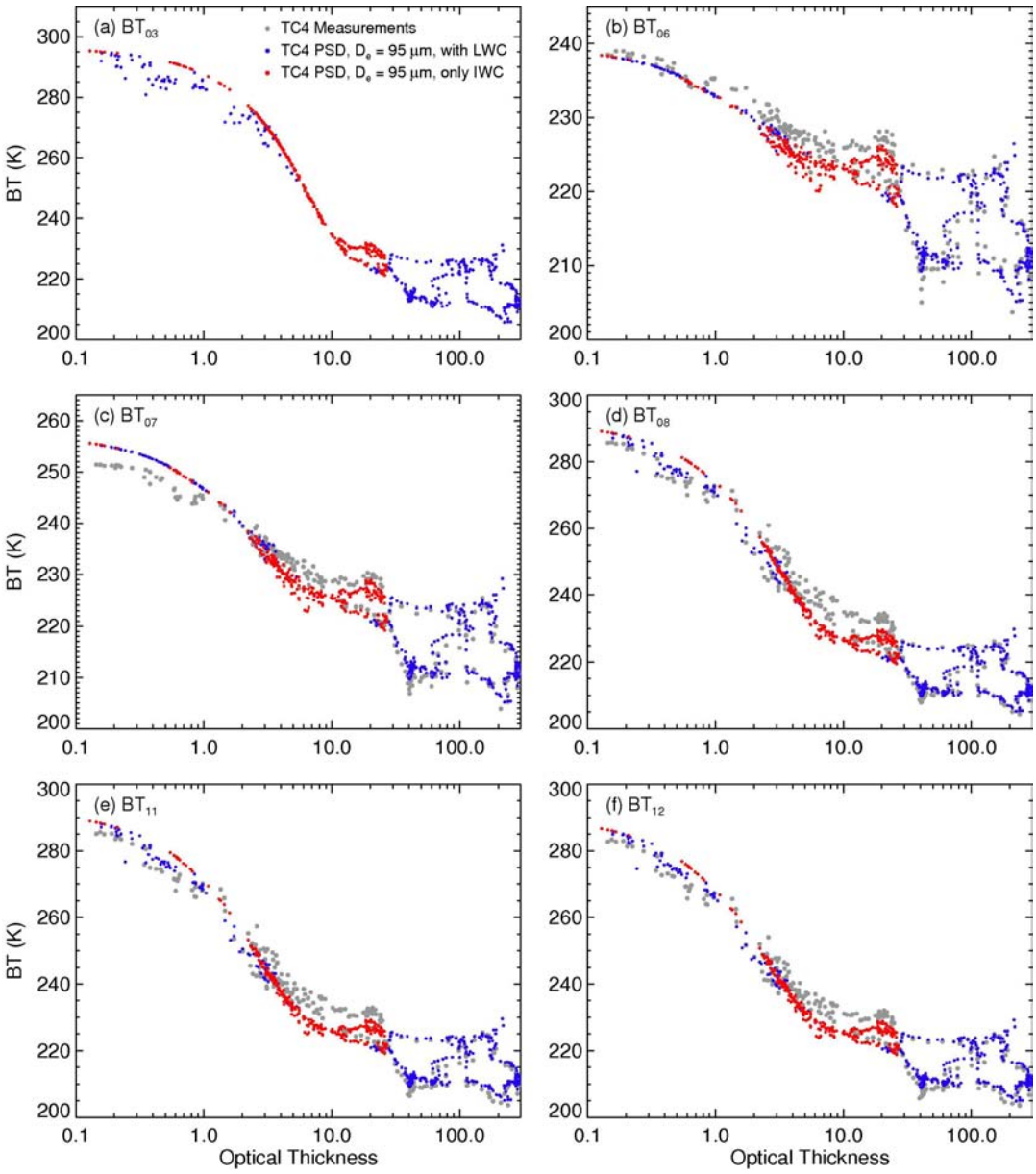

Figure 13. Simulated brightness temperatures at 3.7 and 6.7 μm over the subject cloud system as a function of ice cloud τ using phase transition temperatures of 0°C and -20°C.

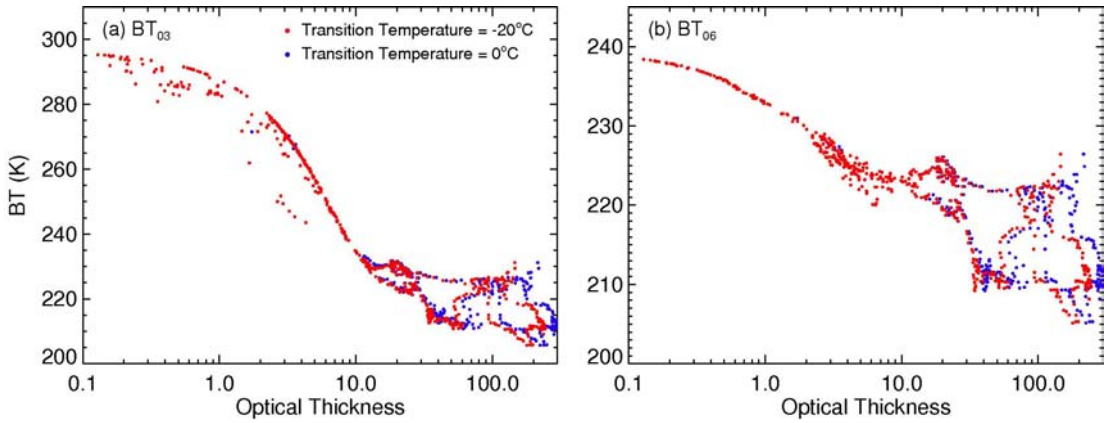

Figure 14. Same as Figure 12, except for brightness temperature differences (BTD).

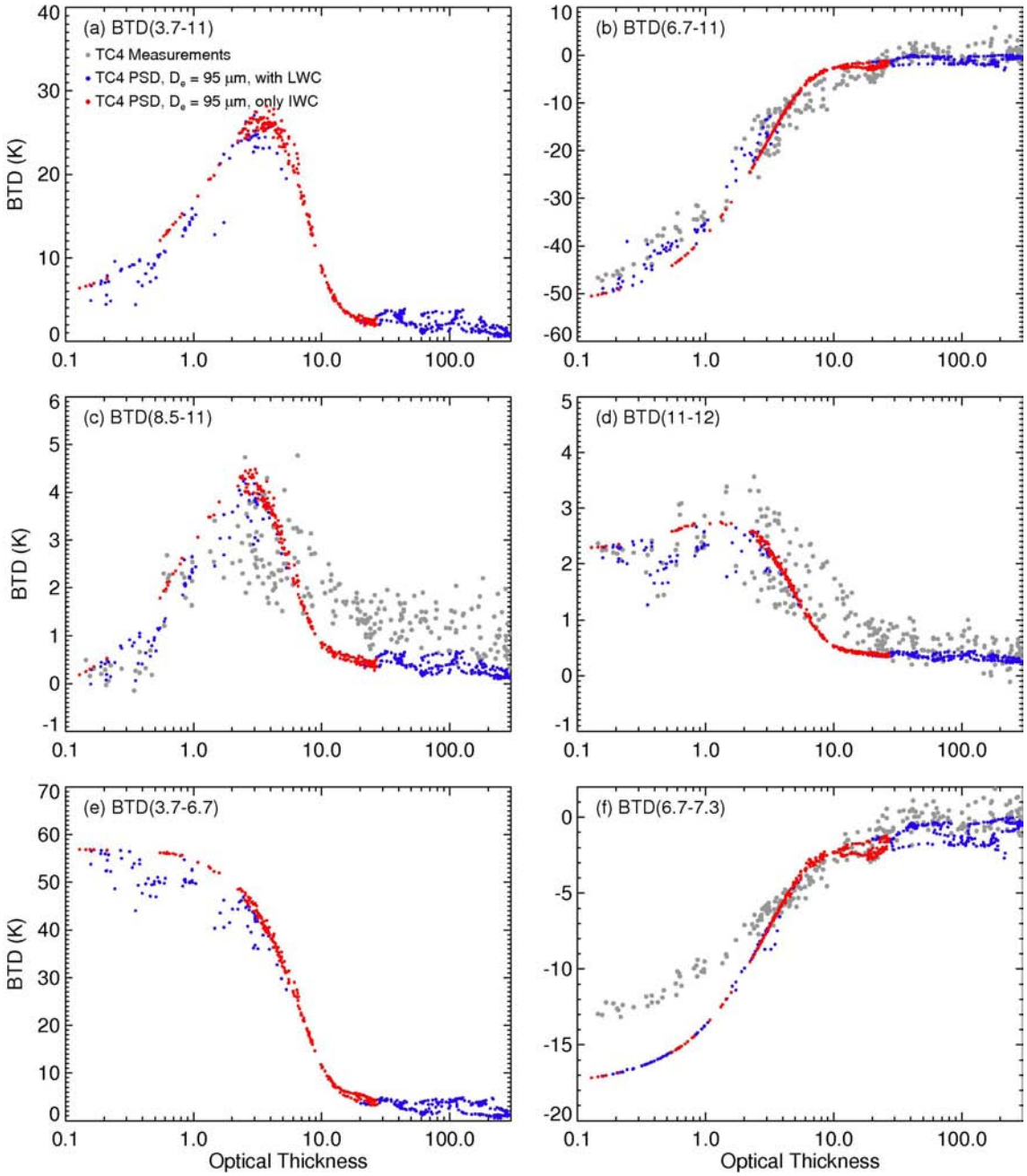

Figure 14 shows the simulated and observed BTDs among the 3.7, 6.7, 7.3, 8.5, 10.8, and 12.0-μm bands over the cloud system as a function of ice cloud τ. As in Figure 12, the BT_{03} measurements are not shown in Figure 14. In general, the simulated values of BTD(6.7-11) (BTD between 6.7 and 10.8-μm bands and others are similarly defined), BTD(8.5-11), BTD(11-12), and BTD(6.7-7.3) are consistent with their respective observations. They are differentially impacted by the presence of low clouds when the ice clouds are optically thin. The water vapor bands at 6.7 and 7.3 μm are affected by upper and middle tropospheric water vapor and above, respectively when the ice clouds are optically thin. This is clearly shown in Figure 14f, which shows that the simulated BTD(6.7-7.3) values differ significantly from the observations when $\tau < 3$, but dramatically decrease as τ increases. Both the simulated and observed BTDs show strong sensitivities to τ of up to 10. Weak sensitivities to τ up to 20 are also found for BTD(3.7-11), BTD(6.7-11), BTD(3.7-6.7) and BTD(6.7-7.3).

Figure 15. Same as Figure 14, except dependence on effective particle size of ice cloud included.

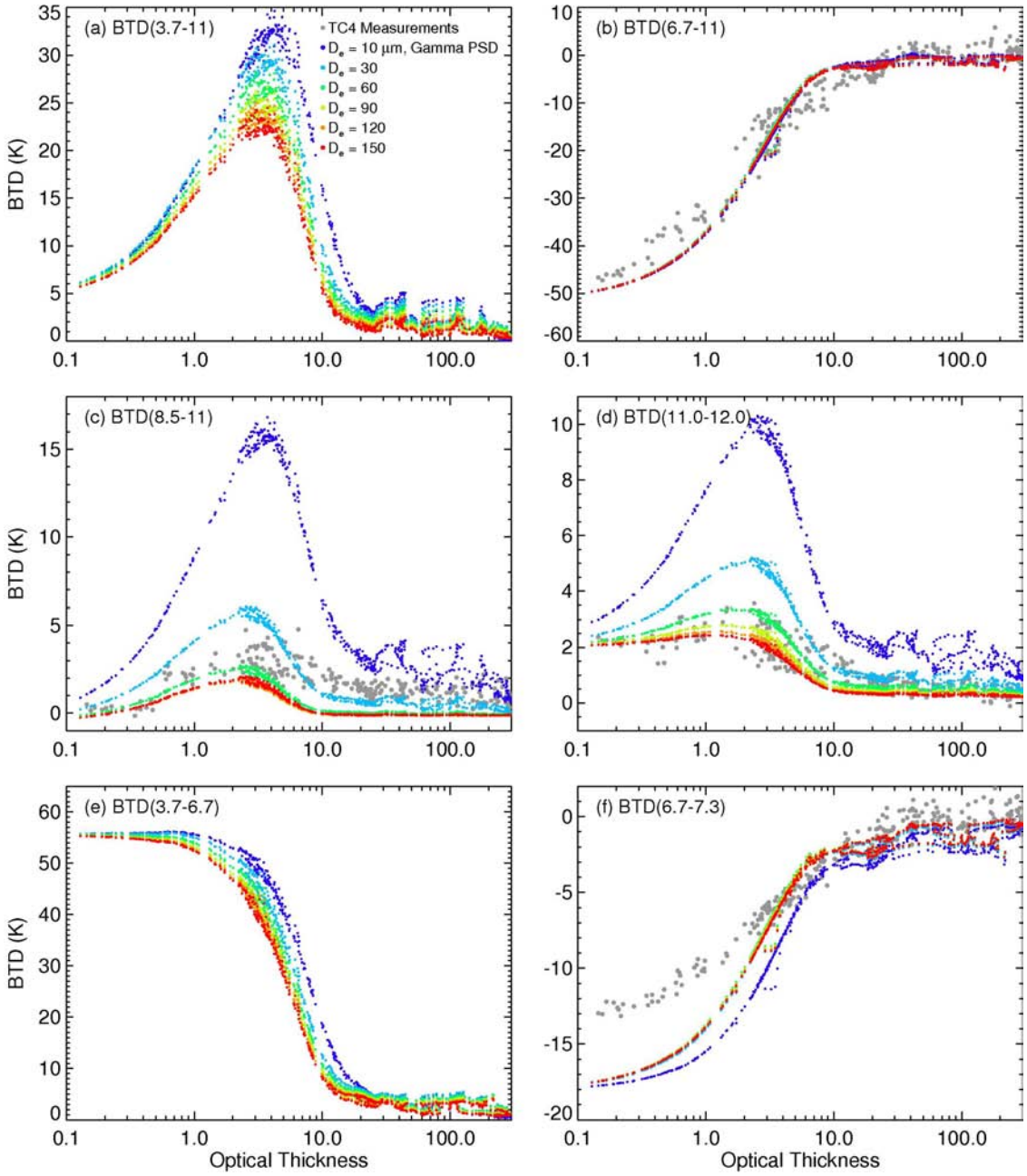

Brightness temperatures for the 3.7, 6.7, 7.3, 8.5, 10.8, and 12.0-μm bands and their BTDs are commonly used to estimate ice cloud D_e. As noted earlier, previous studies of infrared cloud retrievals have been limited mainly to non-opaque ice clouds having $\tau < \sim 6$. Here, the effects of ice particle size D_e on the BTDs and the potential of estimating D_e for optically thick ice clouds are investigated by performing simulations with D_e in the range of 10-150 μm. Figure 15 shows simulated BTDs for various 3.7, 6.7, 7.3, 8.5, 10.8, and 12.0-μm pairs over the subject cloud system as functions of τ and D_e. For these simulations, only ice clouds are involved and the underlying water clouds are not involved. The observed BTDs, except for those for the 3.7-μm band with its reflected solar radiances, are also shown together with these simulations. Consistent with previous studies, BTD(3.7-11), BTD(8.5-11), BTD(11-12), and BTD(3.7-6.7) show strong sensitivity to ice cloud D_e when the ice clouds are non-opaque [11-12] [34]. With τ increasing above ~3, the differences in BTD(3.7-11), BTD(8.5-11), BTD(11-12), and BTD(3.7-6.7) as a function of D_e decrease eventually. BTD(6.7-11) is

Figure 16. Brightness temperatures differences for select pairs of 3.7, 6.7, 8.5, 10.8, and 12.0-μm radiances over the tropical deep convective clouds ($20 < \tau < 100$) as a function of effective particle size D_e. RSD is relative standard deviation.

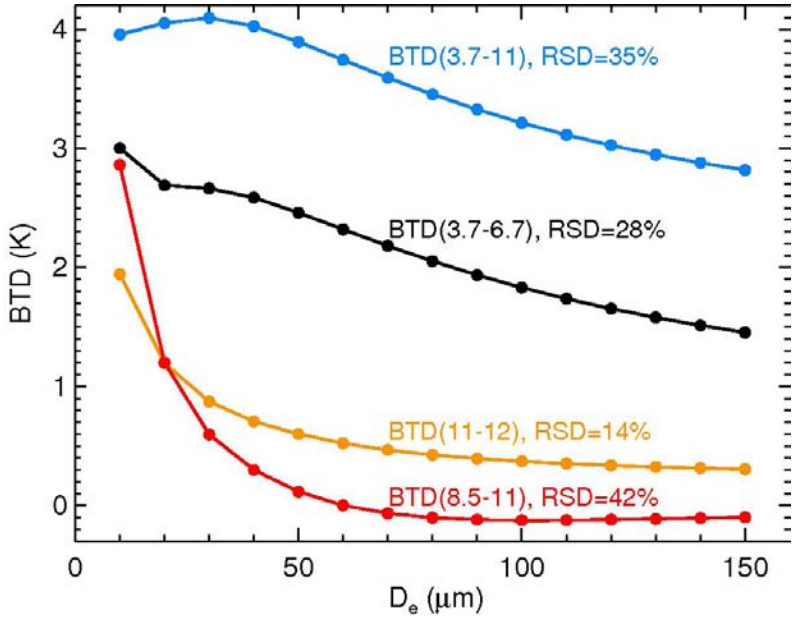

essentially insensitive to D_e, which indicates that it can provide a good estimation of τ, since it increases asymptotically toward zero at $\tau > 20$ in the present simulations. BTD(6.7-7.3) only shows differences for $D_e < 30$ μm. When the opaque ice cloud τ increases, the sensitivity of these BTDs to D_e decreases dramatically. BTD(8.5-11) and BTD(11-12) are only sensitive to small D_e while BTD(3.7-11) and BTD(3.7-6.7) still show weak sensitivity to large values of D_e.

Although BTD(3.7-11), BTD(8.5-11), BTD(11-12), and BTD(3.7-6.7) show significant variability over the deep convective clouds ($\tau > 20$), the general feature of decreasing BTDs with increasing D_e is still apparent. In order to investigate the potential for estimating D_e using these BTDs, the BTDs for each D_e are averaged for ice clouds having τ in the range of 20-100. Figure 16 shows the BTD(3.7-11), BTD(8.5-11), BTD(11-12), and BTD(3.7-6.7) over the tropical deep convective clouds ($20 < \tau < 100$) as a function of D_e. It is evident that BTD(3.7-11) and BTD(3.7-6.7) are sensitive to D_e. BTD(8.5-11) is only sensitive to D_e smaller than 50-70 μm and BTD(11-12) is only sensitive to the smallest D_e values. This feature reveals the potential of estimating small D_e using these BTDs for tropical deep convective clouds during nighttime.

4. Discussion

Simulations of cloud radiance fields necessarily require a considerable number of assumptions about the cloud, humidity, and temperature horizontal and vertical variations. Differences between the observations and simulations in Figs. 14b and 14f are likely due to those assumptions. As noted above, the differences for $\tau < 6$ are likely due to the presence of low or midlevel clouds below thin cirrus clouds. For larger optical depths computed from the CPL and CRS data, the observed water vapor channel BTDs do not appear to reach a distinct asymptote around $\tau = 8$ as seen in the simulations. Rather, the asymptote is not reached until $\tau = 20$ or so. Thus, the vertical variations of D_e, IWC, temperature, and humidity are likely different than assumed and/or higher layer resolution is needed in

the calculations. Given the obvious complexities in the actual structure, however, the results overall are remarkably similar.

The above results suggest that there is useful information about thick ice cloud optical depth and effective particle size in the BTDs between several channels commonly found on operational meteorological satellites. In particular, the 6.7-μm water vapor and the 3.7-μm shortwave-infrared channels, when differenced with the 11-μm channel, appear to be most sensitive to τ and D_e, respectively. If the sensitivities in the example studied here are representative of all thick ice cloud systems, then it should be possible to develop methods to retrieve those parameters at night for cloud having $\tau > 6$.

While it is beyond the scope of this paper to completely evaluate the typicality of the above results, it is useful to determine if the dependencies seen here are, at least, qualitatively evident in satellite imagery. Figure 17 shows imagery over Central America from GOES-12 taken at the same time as the example presented above. The pseudocolor RGB (red: BT_{11}, scale reversed; green: BTD(3.9-11); and blue: 0.65-μm reflectance) and BTD(6.7-11) images are shown in Figs. 17a and 17d, respectively. Figures 17b and 17c depict the effective cloud height Z_c and τ, respectively, derived using the methods

Figure 17. GOES-12 imagery and retrieved cloud properties, 1415 UTC, 5 August 2007.

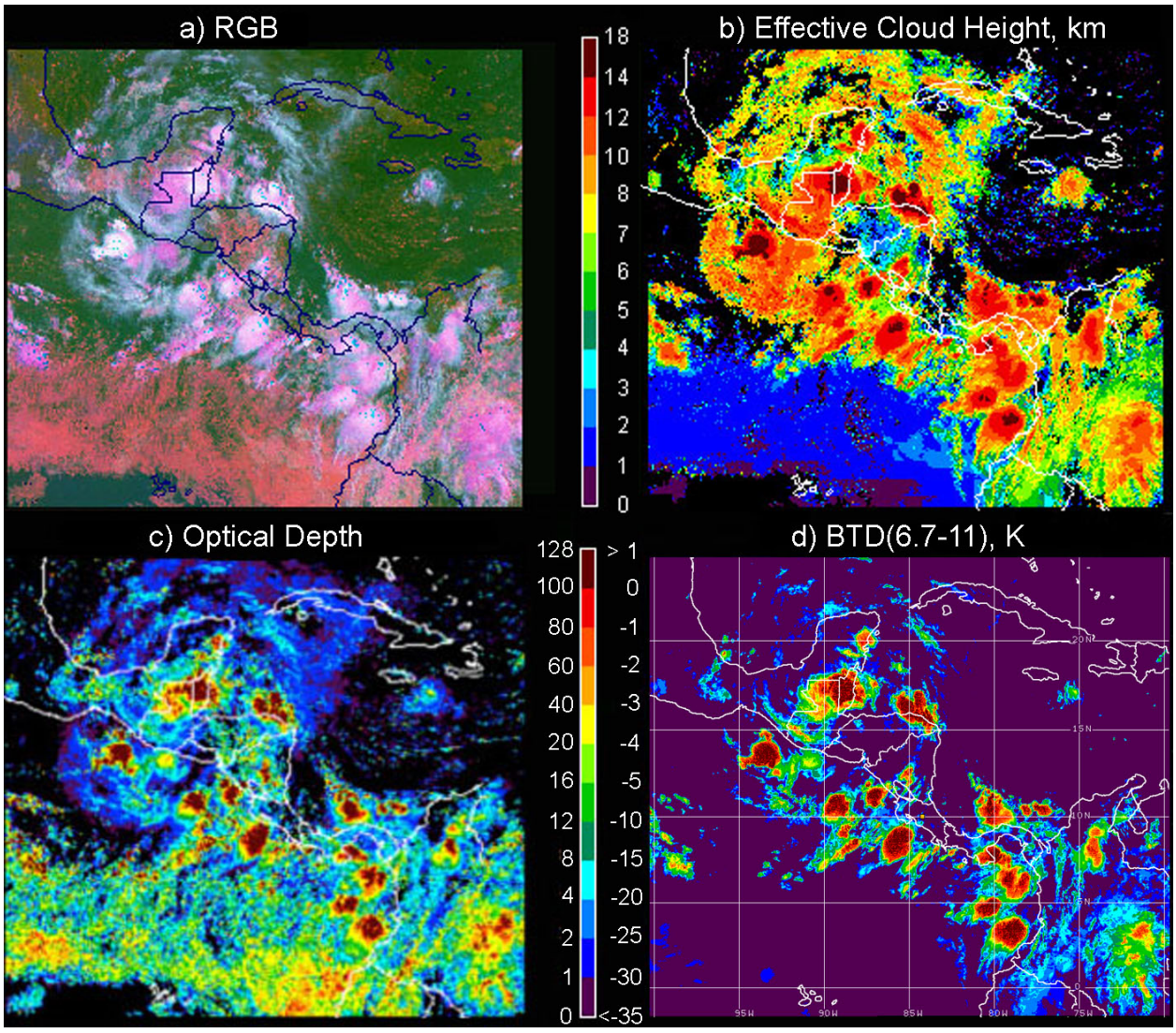

of Minnis et al. [12]. Generally, in these images, wherever Z_c > 6 km and τ > 4, BTD(6.7-11) > -20 K or so. While there is not perfect correlation, some of the large optical depths are caused by thin cirrus over thick stratus, it is clear that the gradients in BTD(6.7-11) correspond, to some extent, to the gradients in τ for the thicker portions of the high clouds.

At night, similar gradients in BTD(6.7-11) are evident around the convective cells in the 1045 UTC GOES-12 imagery for 5 August 2007 (Fig. 18). The correspondence between the highest clouds and the BTD(6.7-11) gradients around the cores is as strong in Figs. 18a, d as that seen in Fig. 16, suggesting similar variations in τ. The imagery also highlights some of the difficulties that will be encountered when trying to use such spectral signals to retrieve τ. The midlevel (5-7 km in Fig. 18b) clouds over the Andes and even some of the marine stratus clouds in the lower left part of the image are also accompanied by some variations in BTD(6.7-11) that approach -20K. With even drier atmospheres over mid- and lower-level clouds in other areas, BTD(6.7-11) will be even closer to 0 K. Thus, other information such as effective cloud height (e.g., Fig. 18b) and other channel BTDs, as well as accurate temperature and water vapor profiles would be needed to unravel the BTD(6.7-11) signal.

Figure 18. GOES-12 imagery and retrieved cloud properties, 1045 UTC, 5 August 2007.

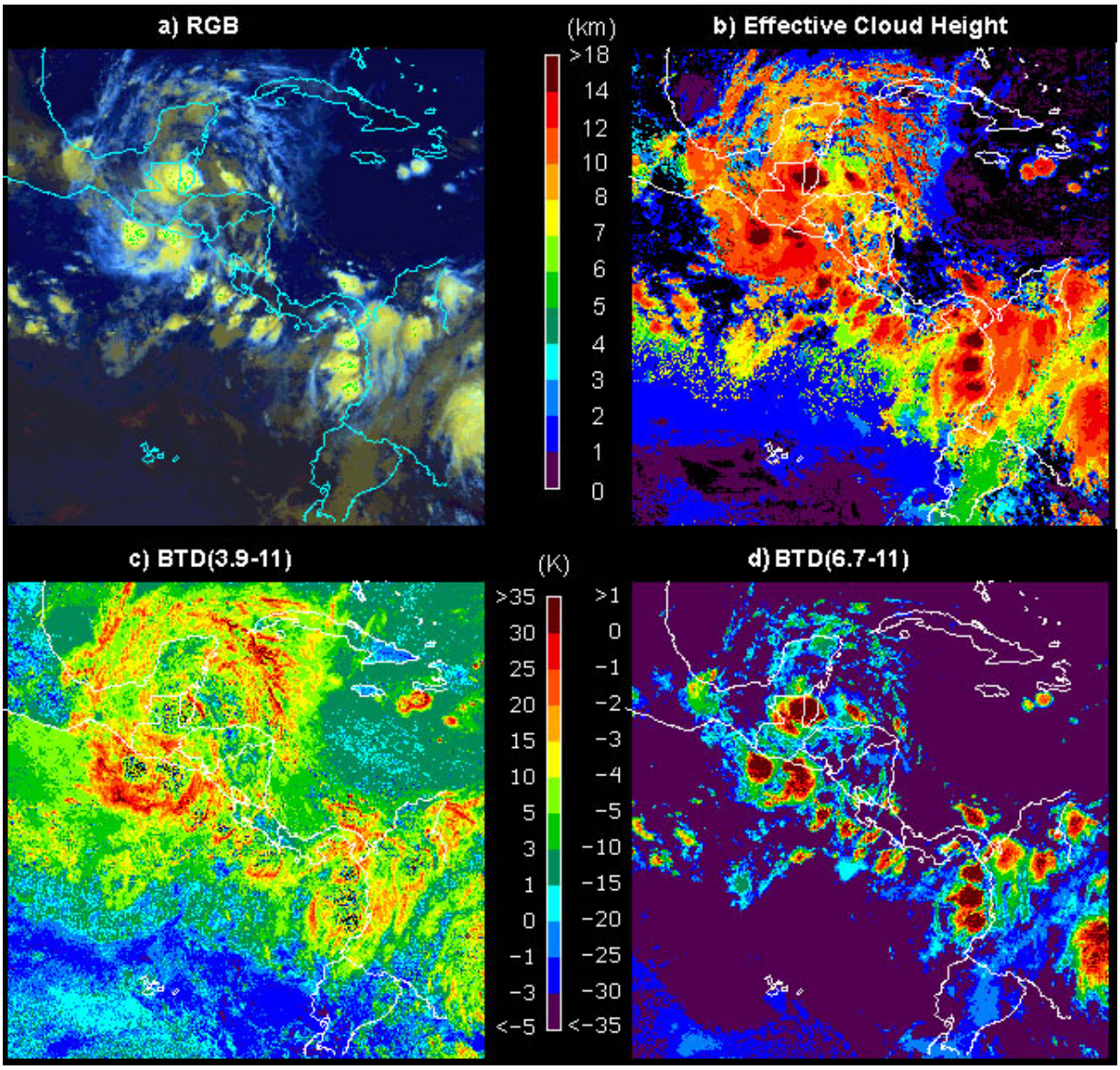

There are considerable variations in BTD(3.9-11) in Fig. 18c with the largest values (> 30 K) occurring in the anvil-generated cirrus. The 3.7 and 3.9-μm channels are similar enough to make some inferences from Fig. 15a. The greatest values likely correspond to smaller values of D_e for $2 < \tau < 8$. As the optical depth increases toward the core, BTD(3.9-11) drops precipitously to < 10 K and eventually becomes noisy over the core because the accuracy of BT_{03} is greatly diminished at the lowest temperatures (< 205 K). The gradient in BTD(3.7-11) over a convective core can be seen more clearly for the developing storms just southwest of Hispaniola. There, BTD(6.7-11) is close to -1K, which would correspond to $30 < \tau < 100$ (Fig. 15b) and the smallest value of BTD(3.7-11) is ~ 5 K, which would correspond to small particles at the cloud top (Fig. 18b). Thus, for all but the coldest clouds, the satellite observations suggest that D_e cloud be retrieved at night for many of the thicker ice clouds.

The case presented in the previous section used a tropical convective system and may have characteristics unlike high clouds in mid-latitudes and polar regions. Figure 19 shows imagery from the Meteosat-9 Spinning Enhanced Visible Infrared Imager (SEVIRI) taken at 1200 UTC, 1 June 2012 over Europe. The RGB image (Fig. 19a) shows baroclinic systems over the eastern and western sides of the domain with stratus clouds between and cirrus clouds over Italy and North Africa. Cloud optical depths retrieved with the methods of Minnis et al. exceed 100 over parts of the eastern system and are greater than 20-40 over portions of the western high clouds [12]. Although the correspondence of BTD(6.7-11) in Fig. 19c with τ is less obvious than seen in Fig. 17, some is still present. This diminished correspondence could be due to the considerable amount of multi-layered clouds occurring in the baroclinic systems and the higher viewing zenith angles for the domain. The variations in τ derived using the 0.65-μm reflectance are due to the total column cloud optical depth, while τ for the upper layer clouds should primarily be responsible for variations in BTD(6.7-11). While this difference in sensitivity could raise some obstacles to retrieving τ at night, it could also provide a means for detecting multilayered clouds and, perhaps, retrieving their properties using an approach similar to that of Chang et al. [85].

The information in the BTD(8.5-11) and BTD(11-12) images in Figs. 19d and 19f, respectively, could also aid in the determination of multilayered cloud conditions and the utility of the BTD(6.7-11) for thick cloud τ retrievals. For example, the large values of BTD(8.5-11) and BTD(11-12) over Italy and North Africa indicate that the high clouds have $\tau < \sim 4$ and small values of D_e. The near-zero values for both channel differences over much of the frontal cloudiness suggest that the ice clouds are opaque and the retrieval of τ using BTD(6.7-11) would apply only to ice clouds. If it is significantly different from the visible channel τ retrieval, then it could be concluded that a multilayered or contiguous, very thick cloud was present. Figure 17f shows the results of applying the 11 and 13.4-μm channel method of Chang et al. to the same image [85]. Most of the clouds classified as thick multilayer or thick high clouds by the Chang et al. technique correspond to areas where BTD(6.7-11) > -15 K [85]. Thus, it appears that even in the absence of the 13.4-μm channel, it may be possible to obtain valuable multilayered cloud information using the 6.7 and 11-μm channels common to all current and most older geostationary satellites.

Figure 19. Meteosat-9 SEVIRI imagery and retrieved cloud properties over Europe, 1200 UTC, 1 June 2012. (a) pseudocolor RGB image, (b) retrieved cloud optical depth, (c) BTD(6.7-11), (d) BTD(8.5-11), and (e) BTD(11-12).

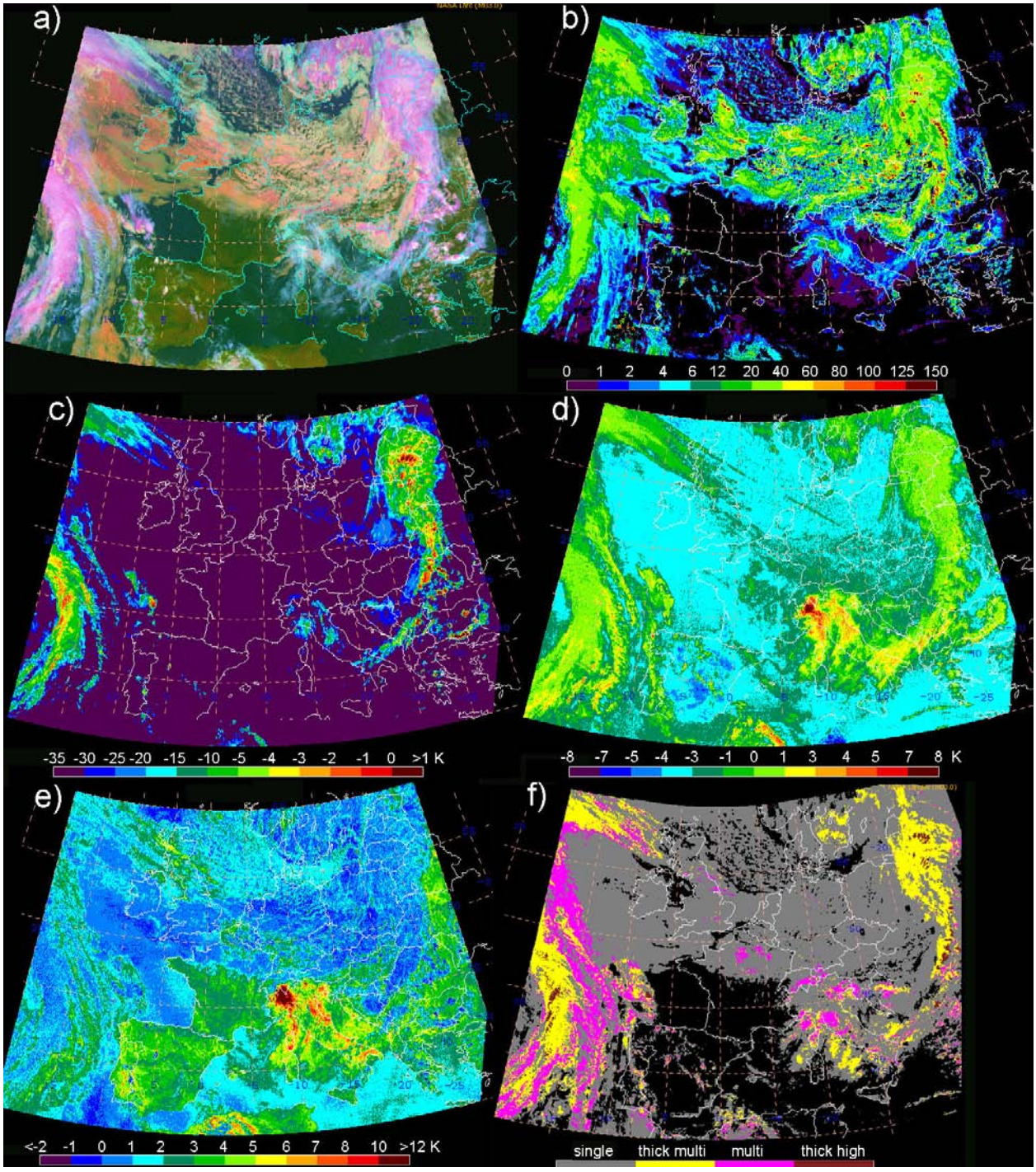

5. Conclusions

With the aid of TC4 aircraft measurements of radiances over a tropical deep convective cloud system and simulations of radiances using *in situ* measurements of cloud properties, this paper has investigated the sensitivities of brightness temperatures for these bands and their differences to ice cloud τ and D_e. Measurements from two aircraft and a surface-based radiosonde were used in a

detailed radiative transfer model to simulate radiances at various MODIS channel bandwidths that would emanate from the top of a deep convective cloud complex. The simulated radiances were compared with radiance measurements taken at a nadir view from two instruments on the ER-2 and adjusted to the MODIS filter functions.

The simulated BTs are generally consistent with the corresponding observations, particularly, for optically thick ice clouds with $\tau > 20$ (i.e., deep convective clouds). The IR radiances emitted from deep convective clouds are essentially the result of contributions from the cloud and atmospheric gaseous absorption and emission above the clouds (upper troposphere), which can be neglected, particularly at the window bands, 3.7, 8.5, 10.8 and 12.0 μm. Both the simulations and observations of these IR brightness temperatures monotonically decrease with increasing ice cloud τ up to ~20. Although, in some instances, significant differences are found in between the absolute values of the simulations and observations, a weak decreasing trend is found with increasing ice cloud τ when τ is above 20. Similar to brightness temperatures, simulated BTDs among these bands generally agree with the observations. Both simulated and observed BTD(3.7-11), BTD(6.7-11), BTD(3.7-6.7), and BTD(6.7-7.3) are sensitive to ice cloud τ up to ~20.

The sensitivity of BTDs to D_e was also investigated. BTD(6.7-11) has no sensitivity to D_e. This feature provides an advantage for estimating ice cloud τ. Consistent with previous studies on estimating ice cloud D_e using IR BTDs, BTD(3.7-11), BTD(8.5-11), BTD(11-12), and BTD(3.7-6.7) show strong sensitivity to D_e of non-opaque ice clouds. With increasing ice cloud τ, the sensitivity becomes weak. Over deep convective clouds ($\tau > 20$), both BTD(3.7-11) and BTD(3.7-6.7) show sensitivity to D_e while BTD(8.5-11) is only sensitive to small D_e that are less than 50-70 μm and BTD(11-12) is sensitive to even smaller D_e.

The simulated results are also generally consistent with satellite observations taken at similar wavelengths and indicate that some combination of these channels, particularly the 3.7, 6.7, and 11-μm channels, could be used for retrieving the optical depth and particle sizes of ice clouds that exceed the typical opaque limit of 6 for cloud optical depth. While many challenges and obstacles would need to be overcome, it may be possible to use such information to provide better quantitative monitoring of clouds over the entire diurnal cycle. Such a capability would aid both climate and weather studies because clouds are an essential component of the radiation and water budgets of the atmosphere both day and night.

Acknowledgments

The authors acknowledge all of them for providing related data for this study. We would like to gratefully thank Hank Revercomb and the S-HIS research team and Sarah T. Bedka for providing the S-HIS measurements, June Wang and Kathryn Young for special processing of the dropsonde data, and L. Li for help on the CRS data used in this paper. The airborne MASTER measurements used in this paper are archived at http://masterweb.jpl.nasa.gov/data/, and the CRS measurements were obtained at http://espoarchive.nasa.gov/archive/arcs/tc4/). This research was supported by the NASA Modeling, Analysis, and Prediction Program, the NASA CERES and TC4 programs, and the NOAA GOES-R Program.

References and Notes

1. Wang, P. H.; Minnis, P.; McCormick, M. P.; Kent, G. S.; Skeens, K. M. A 6-year climatology of cloud occurrence frequency from stratospheric aerosol and gas experiment II observations (1985-1990). *J. Geophys. Res.,* **1996** *101,* 29407–29429.
2. Ramanathan, V.; Collins, W. Thermodynamic regulation of ocean warming by cirrus clouds deduced from observations of the 1987 El Niño. *Nature,* **1991**, *351,* 27–32.
3. Liou, K.-N. Influence of cirrus clouds on weather and climate processes: A global perspective. *Mon. Wea. Rev.,* **1986***, 114,* 1167–1199.
4. Fueglistaler, S.; Dessler, A.E.; Dunkerton, T.J.; Folkins, I.; Fu, Q.; Mote, P.W. Tropical tropopause layer. *Rev. Geophys.,* **2009**, *47,* RG1004, doi:10.1029/2008RG000267.
5. Immler, F.; Krüger, K.; Tegtmeier, S.; Fujiwara, M.; Fortuin, P.; Verver, G.; Schrems, O. Cirrus clouds, humidity, and dehydration in the tropical tropopause layer observed at Paramaribo, Suriname (5.8ºN, 55.2ºW). *J. Geophys. Res.,* **2007,** *112,* D03209, doi:10.1029/2006JD007440.
6. Huang, X.; Su, H. Cloud radiative effect on tropical troposphere to stratosphere transport represented in a large-scale model. *Geophys. Res. Lett.,* **2008**, *35,* L21806, doi:10.1029/2008GL035673.
7. Luo, Z., G.Y. Liu, G.Y.; Stephens, G.L. CloudSat adding new insight into tropical penetrating convection. *Geophys. Res. Lett.,* **2008**, *35,* L19819, doi:10.1029/2008GL035330.
8. King, M.D.; Kaufman, Y.J.; Menzel, W.P.; Tanre, D. Remote sensing of cloud, aerosol, and water vapor properties from the moderate resolution imaging spectrometer (MODIS). *IEEE Trans. Geosci. Remote Sens.,* **1992**, *30,* 2–27.
9. King, M.D.; Menzel, P.; Kaufman, Y.J.; Tanre, D.; Gao, B.-C.; Platnick, S.; Ackerman, S.A.; Remer, L.A.; Pincus, R.; Hubanks, P.A. Cloud and aerosol properties, precipitable water, and profiles of temperature and water vapor from MODIS. *IEEE Trans. Geosci. Remote Sens.,* **2003***, 41,* 442–458.
10. Minnis, P.; Takano, Y.; Liou, K.-N. Inference of cirrus cloud properties using satellite-observed visible and infrared radiances, Part I: Parameterization of radiance fields. *J. Atmos. Sci.,* **1993***, 50,* 1279–1304.
11. Minnis, P.; Garber, D.P.; Young, D.F.; Arduini, R.F.; Takano, Y. Parameterization of reflectance and effective emittance for satellite remote sensing of cloud properties, *J. Atmos. Sci.,* **1998**, *55,* 3313–3339.
12. Minnis, P., et al. CERES Edition-2 cloud property retrievals using TRMM VIRS and Terra and Aqua MODIS data, Part I: Algorithms. *IEEE Trans. Geosci. Remote Sens.,* **2011**, *49*, 4374-4400, doi:10.1109/TGRS.2011.2144601.
13. Rossow, W.B.; Schiffer, R.A. Advances in Understanding clouds from ISCCP. *Bull. Amer. Meteor. Soc.,* **1999***, 80,* 2261–2288.
14. Platnick, S.; King, M. D.; Ackerman, S. A.; Menzel, W. P.; Baum, B. A.; Riédi, J. C.; Frey, R. A. The MODIS cloud products: Algorithms and examples from Terra. *IEEE Trans. Geosci. Remote Sens.,* **2003***, 41,* 459–473.
15. Wylie, D.P.; Jackson, D.L.; Menzel, W.P.; Bates, J.J. Trends in global cloud cover in two decades of HIRS observations. *J. Climate,* **2005***, 18,* 3021–3031.

16. Heidinger, A.K.; Pavolonis, M.J. Gazing at cirrus clouds for 25 years through a split window. Part I: Methodology. *J. Appl. Meteor. Climatol.,* **2009***, 48,* 1110–1116.
17. Heidinger, A.K. Rapid daytime estimation of cloud properties over a large area from radiance distributions. *J. Atmos. Oceanic Technol.,* **2003***, 20,* 1237–1250.
18. Pavolonis, M.J.; Heidinger, A.K.; Uttal, T. Daytime global cloud typing from AVHRR and VIIRS: Algorithm description, validation, and comparisons. *J. Appl. Meteor.,* **2005***, 44,* 804–826.
19. Wielicki, B. A., et al. Clouds and the Earth's Radiant Energy System (CERES): Algorithm overview. *IEEE Trans. Geosci. Remote Sens.,* **1998***, 36,* 1127–1141.
20. Minnis, P., et al. Cloud detection in non-polar regions for CERES using TRMM VIRS and Terra and Aqua MODIS data. *IEEE Trans. Geosci. Remote Sens.,* **2008***, 46,* 3857–3884.
21. Chaboureau, J.-P.; Bechtold, P. Statistical representation of clouds in a regional model and the impact on the diurnal cycle of convection during Tropical Convection, Cirrus and Nitrogen Oxides (TROCCINOX). *J. Geophys. Res.,* **2005**, *110,* D17103, doi:10.1029/2004JD005645.
22. Chaboureau, J.-P.; Tulet, P.; Mari, C. Diurnal cycle of dust and cirrus over West Africa as seen from Meteosat Second Generation satellite and a regional forecast model. *Geophys. Res. Lett.,* **2007***, 34,* L02822, doi:10.1029/2006GL027771.
23. Hong, G.; Yang, P.; Gao, B.-C.; Baum, B.A.; Hu, Y.X.; King, M.D.; Platnick, S. High cloud properties from three years of MODIS Terra and Aqua data over the Tropics. *J. Appl. Meteor. Climatol.,* **2007***, 46,* 1840–1856.
24. Hong, G.; Heygster, G.; Notholt, J.; Buehler, S.A. Interannual to diurnal Variations in tropical and subtropical deep convective clouds and convective overshooting from seven years of AMSU-B measurements. *J. Climate,* **2008***, 21,* 4168–4189.
25. Mitchell, D.L.; d'Entremont, R.P. Satellite retrieval of the liquid water fraction in tropical clouds between -20 and -38°C. *Atmos. Meas. Tech. Discuss.,* **2011***, 4,* 7657-7698.
26. Inoue, T. On the temperature and effective emissivity determination of semi-transparent cirrus clouds by bispectral measurements in the 10 micron window region. *J. Meteor. Soc. Japan,* **1985**, *63,* 88–99.
27. Wu, M.C. A method for remote sensing the emissivity, fractional cloud cover, and cloud top temperature of high-level, thin clouds. *J. Climate Appl. Meteor.,* **1987**, *26,* 225–233.
28. Hong, G.; Yang, P.; Heidinger, A.K.; Pavolonis, M.J.; Baum, B.A.; Platnick, S.E. Detecting opaque and nonopaque tropical upper tropospheric ice clouds: A trispectral technique based on the MODIS 8–12 μm window bands. *J. Geophys. Res.,* **2010***, 115,* D20214, doi:10.1029/2010JD014004.
29. Menzel, W.P.; Richard, F.; Zhang, H.; Wylie, D.P.; Moeller, C.; Holz, R.E.; Maddux, B.; Strabala, K.I.; Gumley L.E. MODIS global cloud-top pressure and amount estimation: Algorithm description and results. *J. Appl. Meteorol. Climatol.,* **2008***, 47,* 1175–1198.
30. Dubuisson, P.; Giraud, V.; Pelon, J.; Cadet, B.; Yang, P. Sensitivity of thermal infrared radiation at the top of the atmosphere and the surface to ice cloud microphysics. *J. Appl. Meteor. Climatol.,* **2008***, 47,* 2545–2560.
31. Hunt, G.E. Radiative properties of terrestrial clouds at visible and infrared thermal window wavelengths, *Q. J. R. Meteorol. Soc.,* **1973***, 99,* 346–369.

32. Baum, B.A.; Frey, R.A.; Mace, G.G.; Harkey, M.K.; Yang, P. Nighttime multilayered cloud detection using MODIS and ARM data. *J. Appl. Meteor.,* **2003***, 42,* 905–919.
33. Lin, X.; Coakley, Jr., J. Retrieval of properties for semitransparent clouds from multispectral infrared imagery data. *J. Geophys. Res.,* **1993***, 98,* 18 501–18 514.
34. Ou, S.C.; Liou, K.-N.; Gooch, W.M.; Takano, Y. Remote sensing of cirrus cloud properties using Advanced Very-High Resolution Radiometer 3.7 and 10.9-μm channels. *Appl. Opt.,* **1993***, 32,* 2171–2180.
35. Hong, G.; Minnis, P.; Doelling, D.R.; Ayers, J.K.; Sun-Mack, S. Estimating effective particle size of tropical deep convective clouds with a look-up table method using satellite measurements of brightness temperature differences. *J. Geophys. Res.,* **2012***, 117,* D06207, doi:10.1029/2011JD016652.
36. Szejwach, G. Determination of semitransparent cirrus cloud temperature from infrared radiances: Application to METEOSAT, *J. Appl. Meteor.,* **1982***, 21,* 384–393.
37. Liou, K.-N.; Ou, S.C.; Takano, Y.; Valero, F.P.J.; Ackerman, T.P. Remote sounding of the tropical cirrus cloud temperature and optical depth using 6.5 and 10.5 μm radiometers during STEP. *J. Appl. Meteor.,* **1990***, 29,* 716–726.
38. Ackerman, S.A.; Strabala, K.I.; Menzel, W.P.; Frey, R.A.; Moeller, C.C.; Gumley, L.E. Discriminating clear sky from clouds with MODIS. *J. Geophys. Res.,* **1998**, *103,* 32141–32157.
39. Liu, Y.; Key, J.; Frey, R.; Ackerman, S.; Menzel, W. Nighttime polar cloud detection with MODIS. *Remote Sens. Environ.,* **2004**, *92,* 181–194.
40. Frey, R. A.; Ackerman, S.A.; Liu, Y.; Strabala, K.I.; Zhang, H.; Key, J.R.; Wang, X. Cloud Detection with MODIS. Part I: Improvements in the MODIS Cloud Mask for Collection 5. *J. Atmos. Oceanic Technol.,* **2008**, *25,* 1057–1072.
41. Lutz, H.J., Inoue, T.; Schmetz, J. Comparison of a split window and a multi-spectral cloud classification for MODIS observations. *J. Meteor. Soc. Japan,* **2003***, 81,* 623–631.
42. Huang, H.-L.; Yang, P.; Wei, H.; Baum, B.A.; Hu, Y.X.; Atonelli, P.; Ackerman, S. A. Inference of ice cloud properties from high spectral resolution infrared observations. *IEEE Trans. Geosci. Remote Sens.,* **2004**, *42,* 842–852.
43. Kahn, B.H.; Eldering, A.; Ghil, M.; Bordoni, S.; Clough, S. A. Sensitivity analysis of cirrus cloud properties from high resolution infrared spectra, Part I: Methodology and synthetic cirrus. *J. Climate,* **2004**, *17,* 4856–4870.
44. Kahn, B.H., Eldering, A.; Clough, S.A.; Fetzer, E. J.; Fishbein, E.; Gunson, M.R.; Lee, S.Y.; Lester, P.F.; Realmuto, V.J. Near micron-sized cirrus cloud particles in high-resolution infrared spectra: An orographic case study. *Geophys. Res. Lett.,* **2003***, 30(8),* 1441, doi:10.1029/2003GL016909.
45. Wei, H.; Yang, P.; Li, J.; Baum, B.A.; Huang, H.-L.; Platnick, S.; Hu, Y.; Strow, L. Retrieval of semitransparent ice cloud optical thickness from Atmospheric Infrared Sounder (AIRS) measurements. *IEEE Trans. Geosci. Remote Sens.,* **2004***, 42,* 2254–2267.
46. Yue, Q.; Liou, K.-N. Cirrus cloud optical and microphysical properties determined from AIRS infrared spectra. *Geophys. Res. Lett.,* **2009**, *36,* L05810, doi:10.1029/2008GL036502.
47. Comstock, J.M., et al. An intercomparison of microphysical retrieval algorithms for upper tropospheric ice clouds. *Bull. Am. Meteoro. Soc.,* **2007***, 88,* 191–204.

48. Toon, O.B., et al. Planning, implementation, and first results of the Tropical Composition, Cloud and Climate Coupling Experiment (TC4). *J. Geophys. Res.,* **2010***, 115,* D00J04, doi:10.1029/2009JD013073.
49. Hook, S.J.; Myers, J.J.; Thome, K.J.; Fitzgerald, M.; Kahle, A.B. The MODIS/ASTER airborne simulator (MASTER) - a new instrument for earth science studies. *Remote Sens. Environ.,* **2001***, 76,* 93–102.
50. King, M.D.; Platnick, S.; Wind, G.; Arnold, G.T.; Dominguez, R.T. Remote sensing of radiative and microphysical properties of clouds during TC4: Results form MAS, MASTER, MODIS, and MISR. *J. Geophys. Res.*, **2010**, *11*, D00J07, doi:10.1029/2009JD013277.
51. Revercomb, H.E., et al., Recent results from two new aircraft-based Fourier transform interferometers: The Scanning High-Resolution Interferometer Sounder and the NPOESS Atmospheric Sounder Testbed Interferometer. *Proc. 8th International Workshop of Atmospheric Science From Space Using Fourier Transform Spectrometry,* Meteo-France, Toulouse, France, **1998**, 1–6.
52. Li, L.; Heymsfield, G.M.; Racette, P.E.; Tian, L.; Zenker, E. A 94 GHz cloud radar system on a NASA high-altitude ER-2 aircraft. *J. Atmos. Oceanic. Technol.,* **2004**, *21,* 1378–1388.
53. McGill, M.J.; Li, L.; Hart, W.D.; Heymsfield, G.M.; Hlavka, D.L.;. Racette, P.E.; Tian, L.; Vaughan, M.A.; Winker D.M. Combined lidar-radar remote sensing: Initial results from CRYSTAL-FACE. *J. Geophys. Res.,* **2004**, *109,* D07203, doi:10.1029/2003JD004030.
54. McGill, M.J.; Hlavka, D.L.; Hart, W.D.; Spinhirne, J.D.; Scott, V.S.; Schmid, B. The Cloud Physics Lidar: Instrument description and initial measurement results, *Appl. Opt.*, **2002**, *41,* 3725–3734.
55. Jensen, E. J., et al. On the importance of small ice crystals in tropical anvil cirrus, *Atmos. Chem. Phys.,* **2009**, *9,* 5321–5370.
56. Lawson, R.P.; O'Connor, D.; Zmarzly, P.; Weaver, W.; Baker, B.A.; Mo, Q.; Jonsson, H. The 2D-S (Stereo) probe: Design and preliminary tests of a new airborne, high-speed, high-resolution imaging probe. *J. Atmos. Ocean. Tech.,* **2006**, *23,* 1462–1477.
57. Field, P.R.; Heymsfield, A.J.; Bansemer, A. Shattering and particle interarrival times measured by optical array probes in ice clouds. *J. Atmos. Ocean. Tech.*, **2006**, *23*, 1357--1371
58. Baumgardner, D.; Jonsson, H.; Dawson, W.; O'Connor, D.; Newton, R. The cloud, aerosol and precipitation spectrometer (CAPS): A new instrument for cloud investigations. *Atmos. Res.,* **2002**, *59-60,* 251–264.
59. Heymsfield, A.J.; Bansemer, A.; Schmitt, C.G.; Twohy, C.; Poellet, M.R. Effective ice particle densities derived from aircraft data. *J. Atmos. Sci.,* **2004**, *61,* 982–1003.
60. Tian, L.; Heymsfield, G.M.; Heymsfield, A.J.; Bansemer, A.; Li, L.; Twohy, C.H.; Srivastava, R.C. A study of cirrus ice particle size distribution using TC4 observations. *J. Atmos. Sci.,* **2010**, *67,* 195–216.
61. Thompson, A.M., MacFarlane, A.M.; Morris, G.A.; Yorks, J.E.; Miller, S.K.; et al. Convective and wave signatures in ozone profiles over the equatorial Americas: Views from TC4 2007 and SHADOZ Convective and wave signatures in ozone profiles over the equatorial Americas: Views from TC4 2007 and SHADOZ. *J. Geophys. Res.*, **2010**, *115*, D00J23, doi:10.1029/2009JD012909.

62. Austin, R.T.; Heymsfield, A.J.;Stephens, G.L. Retrieval of ice cloud microphysical parameters using the CloudSat millimeter-wave radar and temperature. *J. Geophys. Res.,* **2009**, *114,* D00A23, doi:10.1029/2008JD010049.
63. Baedi, R.J.P.; de Wit, J.J.M.; Russchenberg, H.W.J.; Erkelens, J.S.; Baptista, J.P.V.P. Estimating effective radius and liquid water content from radar and lidar based on the CLARE98 data set. *Phys. Chem. Earth B,* **2000**, *25,* 1057–1062.
64. Liu, C.L; Illingworth, A.J. Toward more accurate retrievals of ice water content from radar measurements of clouds. *J. Appl. Meteorol.,* **2000**, *39,* 1130–1146.
65. Marzano, F.S.; Mugnai, A.; Panegrossi, G.; Pierdicca, N.; Smith, E.A.; J. Turk, J. Bayesian estimation of precipitating cloud parameters from combined measurements of spaceborne microwave radiometer and radar. *IEEE Trans. Geosci. Remote Sens.,* **1999**, *37,* 596–613.
66. Skofronick-Jackson, G.M.; Wang, J.R.; Heymsfield, G.M.; Hood, R.; Manning, W.; Meneghini, R.; Weiman, J.A. Combined radiometer-radar microphysical profile estimations with emphasis on high-frequency brightness temperature observations. *J. Appl. Meteorol.,* **2003**, *42,* 476–487.
67. Heymsfield, A.J.; Matrosov, S.; Baum, B. Ice water path–optical depth relationships for cirrus and deep stratiform ice cloud layers. *J. Appl. Meteor.,* **2003**, *42,* 1369–1390.
68. Mishchenko, M.I.; Rossow, W.B.; Macke, A.; Lacis, A.A. Sensitivity of cirrus cloud albedo, bidirectional reflectance, and optical thickness retrieval to ice-particle shape. *J. Geophys. Res.*, **1996**, *101,* 16,973–16,985.
69. Mishchenko, M.I.; Travis, L.D. Capabilities and limitations of a current FORTRAN implementation of the T-matrix method for randomly oriented, rotationally symmetric scatterers. *J. Quant. Spectrosc. Radiat. Transfer,* **1998**, *60,* 309–324.
70. Baran, A.J. On the scattering and absorption properties of cirrus cloud. *J. Quant. Spectrosc. Radiat. Transfer,* **2004**, *89,* 17–36.
71. Baum, B.A.; Heymsfield, A.J.; Yang, P.; Bedka, S.T. Bulk scattering properties for the remote sensing of ice clouds. Part I: Microphysical data and models. *J. Appl.Meteor.,* **2005**, *44,* 1885–1895.
72. Yang, P.; Wei, H.; Huang, H.-L.; Baum, B.A.; Hu, Y.X.; Kattawar, G.W.; Mishchenko, M.I.; Fu, Q. Scattering and absorption property database for nonspherical ice particles in the near through far-infrared spectral region. *Appl. Opt.,* **2005**, *44,* 5512–5523.
73. Kokhanovsky, A.A. *Light Scattering Reviews: Single and Multiple Light Scattering*; Springer-Praxis: Heidelberg/New York, 2006, 493 pp.
74. Kokhanovsky, A.A. *Light Scattering Reviews 4: Single Light Scattering and Radiative Transfer*; Praxis Publishing Ltd.: Chichester, UK, 2009, 534 pp.
75. Kosarev, A.L.; Mazin, I.P. An empirical model of the physical structure of upper layer clouds, *Atmos. Res.,* **1999**, *26,* 213–228.
76. Hong, G. Parameterization of scattering and absorption properties of nonspherical ice crystals at microwave frequencies. *J. Geophys. Res.,* **2007**, *112,* D11208, doi:10.1029/2006JD008364.
77. Baran, A.J. A review of the light scattering properties of cirrus. *J. Quant. Spectrosc. Radiat. Transfer,* **2009**, *110,* 1239–1260.
78. Yang, P.; Wei, H.L.; Baum, B.A.; Huang, H.-L.; Heymsfield, A.J.; Hu, Y.X.; Gao, B.-C. Turner, D.D. The spectral signature of mixed-phase clouds composed of nonspherical ice crystals and

spherical liquid droplets in the terrestrial window region. *J. Quant. Spectrosc. Radiat. Transf.,* **2003**, *79,* 1171–1188.

79. Lee, J.; Yang, P.; Dessler, A.; Baum, B.A.; Platnick, S. The influence of thermodynamic phase on the retrieval of mixed-phase cloud microphysical and optical properties in the visible and near-infrared region. *IEEE Geosci. Remote Sens. Lett.,* **2006**, *3,* 287–291.
80. Ou, S.C.; et al. Retrievals of mixed-phase cloud properties during the National Polar-Orbiting Operational Environmental Satellite System. *Appl. Opt.*, **2009**, *48,* 1452–1462.
81. Mitchell, D.L.; Lawson, R.P.; Baker, B. Understanding effective diameter and its application to terrestrial radiation in ice clouds. *Atmos. Chem. Phys.,* **2011**, *11,* 3417–3429.
82. Kratz, D.P. The correlated k-distribution technique as applied to the AVHRR channels. *J. Quant. Spectrosc. Radiat. Transfer,* **1995**, *53,* 501–517.
83. Kratz, D.P., Rose, F.G. Accounting for molecular absorption within the spectral range of the CERES window channel. *J. Quant. Spectrosc. Radiat. Transfer,* **1999**, *61,* 83–95.
84. Stamnes, K.; Tsay, S.-C.; Wiscombe, W.J.; Jayaweera, K. Numerically stable algorithm for discrete-ordinate-method radiative transfer in multiple scattering and emitting layered media, *Appl. Opt.,* **1998**, *27,* 2502–2509.
85. Hong, G.; Yang, P.; Baum, B.A.; Heymsfield, A.J. Relationship between ice water content and equivalent radar reflectivity for clouds consisting of nonspherical ice particles, *J. Geophys. Res.,* **2008**, *113,* D20205, doi:10.1029/2008JD009890.
86. Chang, F.-L.; Minnis, P.; Khaiyer, M.M.; Sun-Mack, S.; Kato, S. Passive and active remote sensing of multilayer clouds: A look at GOES, MODIS, CALIPSO, CloudSat and ARM SGP observations. Submitted to *J. Geophys. Res.*, **2012**.